

# Miocene initiation and acceleration of extension in the South Lunggar rift, western Tibet: Evolution of an active detachment system from structural mapping and (U-Th)/He thermochronology

Richard H. Styron,<sup>1,2</sup> Michael H. Taylor,<sup>1</sup> Kurt E. Sundell,<sup>1</sup> Daniel F. Stockli,<sup>1,3</sup> Jeffrey A. G. Oalmann,<sup>1</sup> Andreas Möller,<sup>1</sup> Andrew T. McCallister,<sup>1</sup> Deliang Liu,<sup>4</sup> and Lin Ding<sup>4</sup>

Received 21 August 2012; revised 14 May 2013; accepted 28 May 2013.

[1] Ongoing extension in Tibet may have begun in the middle to late Miocene, but there are few robust estimates of the rates, timing, or magnitude of Neogene deformation within the Tibetan plateau. We present a comprehensive study of the seismically active South Lunggar rift in southwestern Tibet incorporating mapping, U-Pb geochronology and zircon (U-Th)/He thermochronology. The South Lunggar rift is the southern continuation of the North Lunggar rift and comprises a ~50 km N-S central horst bound by two major normal faults, the west-dipping South Lunggar detachment and the east-dipping Palung Co fault. The SLD dips at the rangefront ~20°W and exhumes a well-developed mylonite zone in its footwall displaying fabrics indicative of normal-sense shear. The range is composed of felsic orthogneiss, mafic amphibolite, and leucogranite intrusions dated at ~16 and 63 Ma. Zircon (U-Th)/He cooling ages are Oligocene through late Pliocene, with the youngest ages observed in the footwall of the SLD. We tested ~25,000 unique thermokinematic forward models in Pecube against the structural and (U-Th)/He data to fully bracket the allowable ranges in fault initiations, accelerations, and slip rates. We find that normal faulting in the SLR began in the middle Miocene with horizontal extension rates of ~1 mm a<sup>-1</sup>, and in the north accelerated at 8 Ma to 2.5–3.0 mm a<sup>-1</sup> as faulting commenced on the SLD. Cumulative horizontal extension across the SLR ranges from <10 km in the south to 19–21 km in the north.

**Citation:** Styron, R. H., M. H. Taylor, K. E. Sundell, D. F. Stockli, J. A. G. Oalmann, A. Möller, A. T. McCallister, D. Liu, and L. Ding (2013), Miocene initiation and acceleration of extension in the South Lunggar rift, western Tibet: Evolution of an active detachment system from structural mapping and (U-Th)/He thermochronology, *Tectonics*, 32, doi:10.1002/tect.20053.

## 1. Introduction

[2] Tibet is an archetypal example of an orogen undergoing syncontractional extension (Figure 1). Many models of Tibetan and Himalayan orogenesis have been proposed that explain or incorporate east-directed extension, such as

convective removal of lithospheric mantle [e.g., *England and Houseman*, 1988; *Molnar et al.*, 1993], slab rollback in western Pacific subduction zones [*Yin*, 2000], orogenic collapse and radial spreading [e.g., *Dewey et al.*, 1988; *Copley and McKenzie*, 2007], progressive underthrusting of Indian lithosphere [*DeCelles et al.*, 2002; *Copley et al.*, 2011], or other Himalaya-centric models [e.g., *Klootwijk et al.*, 1985; *Styron et al.*, 2011a]. Most of these models either make predictions or rely on estimates of the age of onset of Tibetan and Himalayan extension. Additionally, many of these and other models seek to characterize the nature of deformation in the orogen, such as the debate between a continuum-style [e.g., *England and Houseman*, 1988; *Bendick and Flesch*, 2007] versus block-style deformation of the orogen [e.g., *Avouac and Tapponnier*, 1993; *Meade*, 2007; *Thatcher*, 2007], or the debate between deformation dominantly occurring along the orogen's boundaries [e.g., *Molnar and Tapponnier*, 1975; *Lacassin et al.*, 2004] versus internal deformation [e.g., *Taylor et al.*, 2003; *Searle et al.*, 2011]. These models are similarly reliant upon predictions or estimates of rates and magnitudes of deformation on faults in the orogen.

Additional supporting information may be found in the online version of this article.

<sup>1</sup>Department of Geology, University of Kansas, Lawrence, Kansas, USA.

<sup>2</sup>Now at Department of Earth and Environmental Sciences, University of Michigan, Ann Arbor, Michigan, USA.

<sup>3</sup>Department of Geology, Jackson School of Geosciences, University of Texas, Austin, Texas, USA.

<sup>4</sup>Institute for Tibetan Plateau Research, Chinese Academy of Sciences, Beijing, China.

Corresponding author: R. H. Styron, Department of Earth and Environmental Sciences, University of Michigan, 2534 C.C. Little Building, 1100 North University Avenue, Ann Arbor, MI 48109-1005, USA. (richard.h.styron@gmail.com)

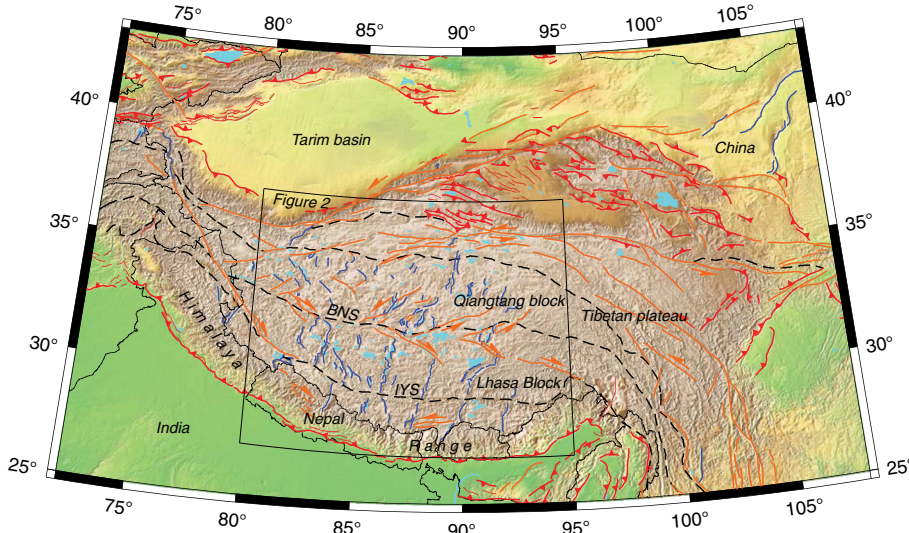


**Figure 1.** Active tectonic map of the Himalayan-Tibetan orogen. Structures are from HimaTibetMap-1.1 [Styron et al., 2010]. Thick red structures = thrust faults. Thin red lines = fold axes. Blue lines = normal faults. Orange lines = strike-slip faults. Dashed black lines = suture zones. BNS = Bangong-Nujiang Suture Zone. IYS = Indus-Yarlung Suture Zone. Topography is from Shuttle Radar Topographic Mission. Lakes are from GSHHS [Wessel and Smith, 1996]. Black box indicates location of Figure 2.

[3] Despite the great interest in Tibetan rifting, only a small number of published studies document the onset of Cenozoic east-west extension within the plateau interior north of the Indus-Yarlung Suture Zone (Figures 1 and 2), in contrast to the relatively well-studied Himalaya (see Lee et al. [2011] for a recent summary). In the eastern plateau, Pan and Kidd [1992] and Harrison et al. [1995] documented Pliocene cooling of the Nyainqntanglha detachment footwall (Figure 2). Harrison et al. [1995] modeled rifting beginning at  $8 \pm 1$  Ma with a fault slip rate of  $3 \text{ mm a}^{-1}$ , a finding that was supported by Kapp et al. [2005a]. A similar age was inferred by Ratschbacher et al. [2011] to the northeast along the same fault system by  $^{40}\text{Ar}/^{39}\text{Ar}$  dating of synkinematic micas from the mylonitic shear zone. Blisniuk et al. [2001] studied a fault zone in the Shuang Hu graben, a local releasing bend in the Muga Purou fault system in central Tibet [Taylor et al., 2003], and dated mineralized fault breccia at  $\sim 13.5$  Ma through Rb-Sr and  $^{40}\text{Ar}/^{39}\text{Ar}$  methods, which they interpreted as the minimum age of rift initiation on the plateau. At face value, these dates suggest that rift inception across the plateau was very diachronous, although the sample size is quite small. Furthermore, these studies do not robustly estimate slip rates on the faults by rigorously testing many slip histories against the data in order to better constrain possible deformation histories.

[4] In order to gain a more thorough understanding of the timing, rates, and magnitude of Cenozoic extension in Tibet, as well as the potential spatial variations in extension, more data are needed, especially for western Tibet. This study presents structural and neotectonic mapping, zircon (U-Th)/He (zHe) thermochronology, and zircon U-Pb analysis of the little-known South Lunggar rift (SLR) in the western Lhasa block of Tibet. We document a large ( $>50$  km along strike) and active north-trending rift containing both high- and low-angle normal faulting. The footwall of the low-angle normal fault displays a

well-developed mylonitic shear zone and is interpreted as a metamorphic core complex. Data collection was combined with extensive three-dimensional (3-D) thermokinematic modeling ( $\sim 25,000$  forward models) to test possible deformation histories against the structural and thermochronometric observations. These results indicate up to 20 km E-W extension starting in the early to middle Miocene, at moderate rates ( $1\text{--}3 \text{ mm a}^{-1}$ ) following a late Miocene acceleration. Significant along-strike variability in fault geometry, slip rate, and net displacement exist as well. In addition to providing new information on extension in SW Tibet, our results have implications for the thermal state of the Tibetan crust. Furthermore, the observations of low-angle normal “detachment” faulting and large thermochronometric data collection allow for testing of various geometric models of detachment faulting.

### 1.1. Style and Evolution of Detachment Faulting

[5] Low-angle ( $<30^\circ$  dip) normal “detachment” faults, often exhibiting several to tens of kilometers of extension, have been mapped throughout the world over the past 30 years [e.g., Wernicke, 1995]. As these structures are not well understood due to the apparent conflict between their dip angle and standard Andersonian rock mechanical theory [e.g., Anderson, 1951] predicting normal fault dips of  $\sim 60^\circ$  and fault locking at low angles, much effort has been put into resolving the contradiction of Andersonian fault theory with field [e.g., Lee et al., 1987; Yin and Dunn, 1992], geophysical [Abers et al., 2002; Morley, 2009], and geodetic [e.g., Hreinsdottir and Bennett, 2009; Niemi et al., 2004] observations. These studies often focus on the geometry of the detachment at depth, and whether faulting initiated at low angle or was first high angle and later rotated to a low angle [e.g., Spencer, 1984; Wernicke and Axen, 1988]. Prominent models include planar, low-angle fault initiation [e.g., Wernicke, 1981]; the “rolling-hinge” model, where the very

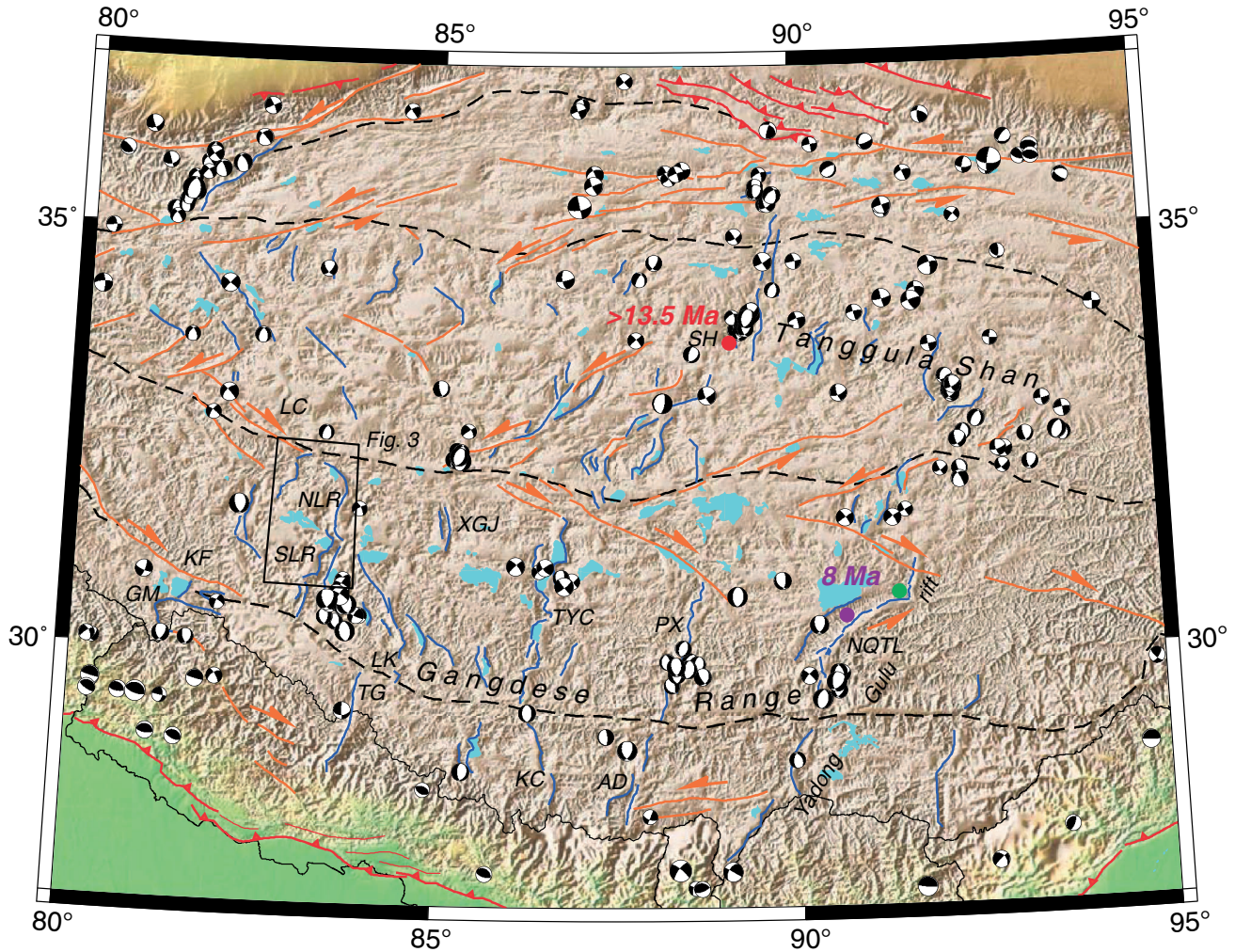


**Figure 2.** Active structures of central and southern Tibet. Map symbology is the same as in Figure 1. Earthquake focal mechanisms are from Global CMT ([www.globalcmt.org](http://www.globalcmt.org)) from 1 Jan 1976 to 20 Mar 2012 above 80 km depth. SH = Shuang Hu graben. LC = Lamu Co fault. NLR = North Lunggar rift. SLR = South Lunggar rift. XGJ = Xianggangjiang rift. LK = Lopukangri rift. TYC = Tangra Yum Co Rift. PX = Pumqu-Xainza rift. NQTL = Nyainqntanglha rift. KF = Karakoram fault. GM = Gurla Mandhata rift. TG = Thakkhola graben. KC = Kung Co rift. AD = Ama Drime rift. Purple circle marks study locations of Pan and Kidd [1992], Harrison et al. [1995] and Kapp et al. [2005a, 2005b]. Green circle marks study location of Edwards and Ratschbacher [2005]. Red circle marks study location of Blisniuk et al. [2001]. Black rectangle indicates location of our mapping in the Lunggar rift (Figure 3).

shallow and very deep parts of the detachment fault are low angle, but the majority of slip within the seismogenic crust occurs at a moderate to high angle [e.g., Axen and Bartley, 1997]; and antilistic models, where the detachment fault monotonically steepens with depth [e.g., Buck, 1988].

[6] Many of the canonical field studies of detachment faults focused on the Cordillera of western North America (indeed, the typically sheared and metamorphosed antiformal footwalls of detachment faults were initially known as “Cordilleran” metamorphic core complexes [Crittenden et al., 1980], now less parochially “metamorphic core complexes” or more simply “core complexes”), which were generally active in the late Cretaceous through Miocene [e.g., Lister and Davis, 1989]. Therefore, few studies [e.g., Daczko et al., 2011; Kapp et al., 2005a; Kapp et al., 2008] have been done on active structures, where

considerably more certainty exists on the geometric and geodynamic context, such as the thickness, strain rate, and thermal state of the crust and upper mantle.

[7] However, computational simulations of detachment faulting and core complex development are numerous. Though there has been significant variability in the modeling approach, the results typically show detachment faulting to form preferentially in areas of hot, thick crust capable of ductile flow at depth [e.g., Buck, 1991; Rey et al., 2009]. These studies also uniformly show the flexural or isostatic “back” rotation of the footwall away from the detachment fault and hanging wall, leading to an updip shallowing of the fault dip, i.e., an “antilistic” fault geometry [e.g., Buck, 1988; Rey et al., 2009; Tirel et al., 2008; Wdowinski and Axen, 1992]. In models that do not specify an initial detachment geometry, some material heterogeneity is often

needed to initially localize deformation; this is typically a magmatic intrusion [e.g., *Brun et al.*, 1994; *Tirel et al.*, 2008], which is compelling because of the strong association of magmatism and core-complex formation [e.g., *Armstrong and Ward*, 1991].

[8] Thermochronologic techniques have proven invaluable in understanding the rate and style of deformation in a variety of tectonic settings, especially in extensional regions, where progressive downdip exhumation of a normal fault footwall often leaves a clear thermal signature [e.g., *Stockli*, 2005]. Thermochronologic data in normal fault footwalls are typically interpreted in age versus elevation or age versus downdip distance plots, often by the fitting of linear regression trend lines [e.g., *Fitzgerald et al.*, 2009; *Mahéo et al.*, 2007]. However, this method makes questionable assumptions about the thermal state of the crust, particularly that the geothermal gradient is constant with depth and does not change during faulting, and radiogenic heating is not significant. These assumptions have been shown to be inaccurate enough to cause erroneous interpretations [*Ehlers et al.*, 2001; *Ehlers*, 2005]. Additionally, structural complications such as progressive rotation of the footwall during extension may distort the geometrical relationship of the samples to horizontal geotherms; these complications have to be well constrained [e.g., *Stockli et al.*, 2002], or ignored. Furthermore, simple regression lines are rarely weighted by age uncertainty, thereby failing to take this important age information into account.

[9] Advances in 2-D and 3-D thermokinematic modeling [e.g., *Harrison et al.*, 1995; *Ketcham*, 1996; *Braun*, 2003; *Ehlers et al.*, 2001] have enabled the use of complicated fault geometries and dynamic, nonlinear geotherms incorporating radiogenic heating. Furthermore, iterative methods [e.g., *Campani et al.*, 2010; *Ketcham*, 2005] allow for model fitting that incorporates formal uncertainties in thermochronometer data, producing much more robust interpretations than previously possible.

[10] Many studies of Himalayan and Tibetan rifting have found evidence of active detachment faulting [e.g., *Harrison et al.*, 1995; *Jessup et al.*, 2008; *Kapp et al.*, 2005a; *Kapp et al.*, 2008; *Murphy et al.*, 2002; *Pan and Kidd*, 1992; *Robinson et al.*, 2004], consistent with predictions of detachment fault formation in hot, thick crust [e.g., *Buck*, 1991]. Detachment faults have been mapped in both the NRL and SLR [*Kapp et al.*, 2008; *Styron et al.*, 2011b], and are interpreted to be active. The identification of rapidly exhumed midcrustal rocks in the detachment footwalls suggests that extension is locally very significant and that faults are of significance to deformation of the Tibetan plateau. The structural and thermochronological work presented here on the SLR give both an understanding of the rates and timing of western Tibetan extension and a picture of core-complex activity in a hot and thick orogen.

## 1.2. Regional Geology

### 1.2.1. Preextensional Geology

[11] The southern margin of Eurasia has been tectonically active throughout the Phanerozoic. This activity mostly consists of the successive accretion of multiple terranes that now compose the Tibetan plateau. Accretion of these terranes is generally assumed to young southward, with docking of the Qilian and Kunlun terranes in the Paleozoic, the Qiangtang terrane in the early-mid-Mesozoic, and the Lhasa terrane in

the mid-late Mesozoic (forming the Bangong-Nujiang Suture Zone, Figure 1) [*Yin and Harrison*, 2000]. The late Cretaceous to early Eocene saw the beginning of India's ongoing collision with the Lhasa terrane along the Indus-Yarlung Suture Zone [*Ding et al.*, 2005], creating much of the crustal shortening observed today.

[12] Shortening in central Tibet began in the late Jurassic [*Murphy et al.*, 1997] or early Cretaceous [*Kapp et al.*, 2005b] associated with the underthrusting of the Lhasa terrane beneath the Qiangtang terrane [e.g., *Yin and Harrison*, 2000; *Kapp et al.*, 2007]. Shortening, accompanied by magmatism, continued throughout the Lhasa terrane until the Paleocene [*Murphy et al.*, 1997; *Kapp et al.*, 2005b, 2007]. Thin-skinned thrust sheets composed of Paleozoic strata were thrust over Mesozoic strata (and vice versa) in the south-central Lhasa terrane and were sporadically intruded by granites throughout the Cretaceous [*Murphy, et al.*, 1997]. During the mid to late Cretaceous, subduction of Neothethyan lithosphere underneath the southern Lhasa terrane produced the Gangdese magmatic arc [e.g., *Ding et al.*, 2003].

[13] Following the onset of India's collision, shortening generally ceased in the interior of the Lhasa terrane (inferred from the widespread and essentially flat-lying early Tertiary Linzizong volcanic rocks) [*Murphy et al.*, 1997], but was still active until ~20 Ma on its northern and southern margins [*DeCelles et al.*, 2011; *Kapp et al.*, 2005b, 2007; *Yin et al.*, 1994] as well as in northern Tibet [e.g., *Lease et al.*, 2011]. Several hundred kilometers of shortening were accommodated in the Himalaya at this time, as well [*DeCelles et al.*, 2002; *Robinson et al.*, 2006; *Murphy*, 2007]. Synconvergent extension in the direction of plate convergence occurred episodically throughout the Oligocene and early Miocene, expressed as activity on the north-dipping South Tibetan Detachment system [*Burg and Chen*, 1984; *Burchfiel and Royden*, 1985] and the development of the South Kailas Basin between the Gangdese arc and the thrusts of the Indus-Yarlung Suture Zone [*DeCelles et al.*, 2011; *Zhang et al.*, 2011].

[14] In the middle to late Miocene, a dramatic change in the style of deformation in the Himalaya and Tibet occurred. Activity on the Main Central Thrust and South Tibetan Detachment, the dominant early Miocene structures in the Himalaya, was significantly reduced if not halted altogether [e.g., *Murphy et al.*, 2002; *Leloup et al.*, 2010] while the dominant zone of Himalayan shortening propagated south [*Meigs et al.*, 1995; *DeCelles et al.*, 2001]. At this time, the High Himalaya began arc-parallel extension along structures cutting the Main Central Thrust and South Tibetan Detachment [*Thiede et al.*, 2006; *Murphy, et al.*, 2002; *Styron et al.*, 2011a; *Garzione et al.*, 2003; *Lee et al.*, 2011; *Jessup et al.*, 2008; *Kali et al.*, 2010; *Leloup et al.*, 2010]. Within the central and southern Tibetan plateau, shortening via folding and thrusting essentially ceased and an ongoing phase of east-west extension began [*Lee et al.*, 2011; *Kapp et al.*, 2008], with ongoing shortening, observed geodetically [e.g., *Zhang et al.*, 2004] ostensibly accommodated on NE- and NW-striking V-shaped conjugate strike-slip faults in central Tibet [*Taylor et al.*, 2003; *Yin and Taylor*, 2011].

### 1.2.2. Neogene Rifts in Tibet

[15] Neogene extension in Tibet is characterized by roughly north-trending graben in the central Lhasa and Qiangtang terranes [e.g., *Armijo et al.*, 1986; *Blisniuk et al.*,

2001] (Figures 1 and 2). These graben are often linked to V-shaped conjugate strike-slip faults emanating from the Bangong-Nujiang Suture zone [e.g., *Taylor et al.*, 2003], although in some cases, such as small graben in the Tanggula Shan and Gangdese Shan, extension may be isolated to areas of high topography (Figure 2). The southern Lhasa terrane contains five major rifts that essentially span the north-south length of the Lhasa terrane, and several subordinate rifts. From east to west, the major rifts are the Yadong-Gulu rift (this rift cuts from the Himalaya to the Bangong-Nujiang suture; the main segment of the rift through the Lhasa block is called the Nyainqntanglha rift [*Pan and Kidd*, 1992; *Kapp et al.*, 2005a]), the Pumqu-Xainza rift [*Armijo et al.*, 1986; *Hager et al.*, 2006], the Tangra Yum Co rift [*Dewane et al.*, 2006], and the Lunggar rift [*Kapp et al.*, 2008, this study]. Subordinate rifts include an unnamed and unstudied (to our knowledge), but seismically active (Figure 2) rift to the west of the Lunggar rift, the Lopukangri rift [*Murphy et al.*, 2010] to the southeast of the Lunggar rift, the Xiagangjiang rift to the east of the North Lunggar rift (NLR) [*Volkmer et al.*, 2007], and numerous small graben throughout the western Gangdese range [e.g., *Yin*, 2000] (Figures 1 and 2).

[16] Some estimates have been made of net horizontal extension across the plateau. *Armijo et al.* [1986] estimated <3–4 km extension across the Yadong-Gulu and Pumqu-Xainza rifts and extrapolate to suggest roughly 20 km extension across the plateau, assuming these rifts are representative of all major Tibetan rifts. More recently, *Kapp et al.* [2005a], informed by modern ideas of detachment faulting and continental extension, studied the Nyainqntanglha segment of the Yadong-Gulu rift. They estimated a minimum of 8 km fault slip based on the downdip length of the detachment fault's mylonitic shear zone and combine structural and thermobarometric data to suggest 21–26 km of fault slip, assuming the detachment fault slipped at 35° dip. Given this fault dip, their corresponding extension estimates would be 17–21 km based on all results with a minimum of 6.5 km. *Taylor et al.* [2003] suggest ~48 km of total right-lateral slip along the southern, right-slip faults in the conjugate fault zone along the Bangong-Nujiang suture that link into south Tibetan graben (i.e., west of the Jiali fault), based on mapping and remote sensing interpretation of the Lamu Co and Riganpei Co faults. Slip on these faults may be comparable to extension in the linked graben (Figures 1 and 2). Preliminary mapping in the Tangra Yum Co [M. Taylor, unpublished mapping] and Pum Qu-Xainza rifts [C. Hager, personal electronic communication] suggests less than 10 km for each rift.

[17] The Lopukangri rift to the southeast of the SLR (Figure 2) is a complex fault system interpreted either as part of the trailing end of an extensional imbricate fan in a fault system extending from the Lamu Co fault through the Lunggar rift and southeastward into the Gangdese range, or as a more prominent member of a series of crustal tears with the same geographic extent [*Murphy et al.*, 2010; *Sanchez et al.*, 2013]. Based on the work of *Sanchez et al.*, 2013 and our preliminary field observations, the Lopukangri rift has a long northern segment, with a west-dipping, moderate-angle range-bounding normal fault. Although throw on this fault has not been enough to exhume basement in its footwall, the fault has extremely large normal fault scarps, offsetting Quaternary alluvium by up to 350 m vertically and locally

display triangular facets several tens of meters high, suggesting that this segment of the rift is reasonably active. To the north of the rift proper is a rangefront fault striking NW that is interpreted as an oblique slip (dextral-normal) fault that terminates to the NW near the central Lunggar rift and may transfer slip from the NLR to the Lopukangri rift. The southern segment of the Lopukangri rift cuts the southern slopes of the Gangdese range, offsetting contractional structures associated with the Indus-Yarlung Suture Zone by ~15 km [*Murphy et al.*, 2010; *Sanchez et al.*, 2013].  $^{40}\text{Ar}/^{39}\text{Ar}$  dating of the footwall of the southern Lopukangri rift suggests rifting began at ~15 Ma [*Sanchez et al.*, 2013].

### 1.3. Lunggar Rift

[18] The Lunggar rift is a major north-trending rift in the western Lhasa terrane [*Armijo et al.*, 1986; *Kapp et al.*, 2008; *Elliott et al.*, 2010] (Figures 2 and 3). It is kinematically linked in the north to the Lamu Co right-lateral strike-slip fault, part of the V-shaped conjugate fault system running along the Bangong-Nujiang Suture Zone [*Taylor et al.*, 2003]. The rift is over 150 km along strike and made up of northern and southern segments separated by an accommodation zone (Figure 3). The northern segment, or the NLR (called the Lunggar rift by *Kapp et al.* [2008] and *Woodruff et al.* [2013]), consists of an east-dipping low-angle detachment fault separating a narrow (<10 km wide) supradetachment basin from an elevated footwall composed of variably deformed granitoids, orthogneiss, and metamorphosed Paleozoic sedimentary rocks. The detachment is inactive at the rangefront, as indicated by unfaulted moraine and alluvial material overlying the fault trace. However, both east and west-dipping normal faults offset Quaternary alluvium in the supradetachment basin and are parallel to the range-bounding detachment, suggesting they sole into the detachment at depth [*Kapp et al.*, 2008]. Relief in the NLR approaches 2 km, and maximum footwall elevations are ~6500 m. The accommodation zone between the NLR and SLR consists of a less-elevated (peak elevations generally <6000 m) footwall made up of the Cretaceous thin-skinned thrust belt that forms the preextensional surface in adjacent regions [*Murphy et al.*, 1997].

[19] The SLR (Figure 4) is made up of a central horst block, the Surla Range, which is bounded on both the east and west by normal faults. Well-developed basins are found on both sides of the Surla Range. Quaternary cumulative fault scarps on flanks of the Surla Range and active seismicity indicate that extension in the SLR is ongoing. The Swedish explorer Sven Hedin was likely the first Westerner to describe the geography and geology of the SLR during his passage through in June, 1908 [*Hedin*, 1909]. He noted the extensive glaciation and wide distribution of granite boulders in the western rift valley. He also described feeling moderate ground shaking due to an earthquake at approximately 9:30 PM (local time) on 28 June 1908 while in Sailipu, a short distance to the west. To our knowledge, this is the first field geologic study of the SLR since Hedin's.

## 2. Bedrock and Surficial Geology of the SLR

### 2.1. Bedrock Units

[20] The Surla Range in our map area is dominantly composed of amphibolite-grade metamorphic rocks (**ma**) and

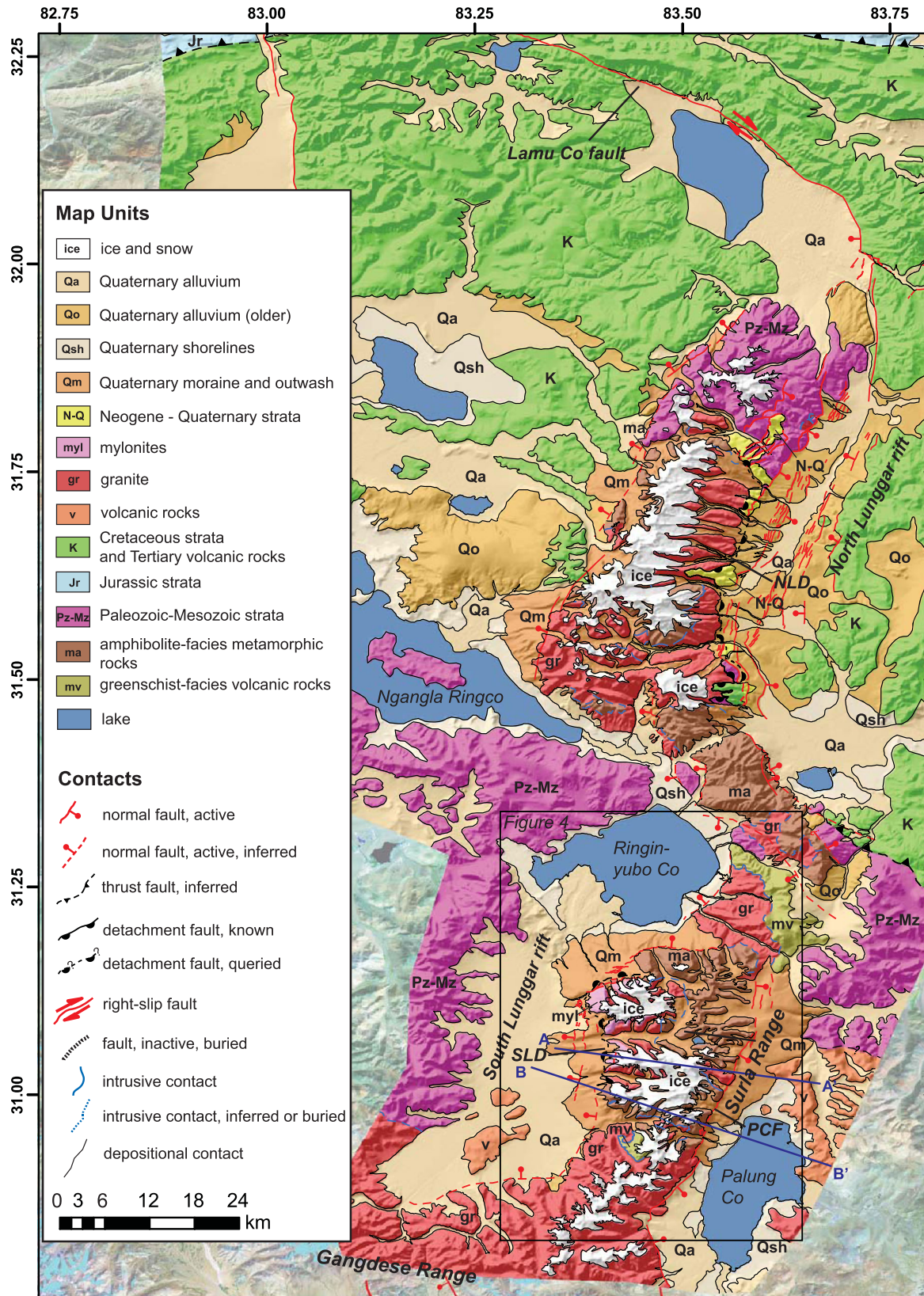


**Figure 3.** Bedrock and Quaternary geologic Map of the North and South Lunggar rifts and Lamu Co fault. Mapping of North Lunggar rift modified from Kapp et al. [2008] and our field observations. Mapping of Lamu Co fault modified from Taylor et al. [2003]. NLD=North Lunggar detachment. SLD=South Lunggar detachment. PCF=Palung Co fault. See Figure 2 for location. Cross-section lines A-A' and B-B' are also shown. Black box indicates location of Figure 4.

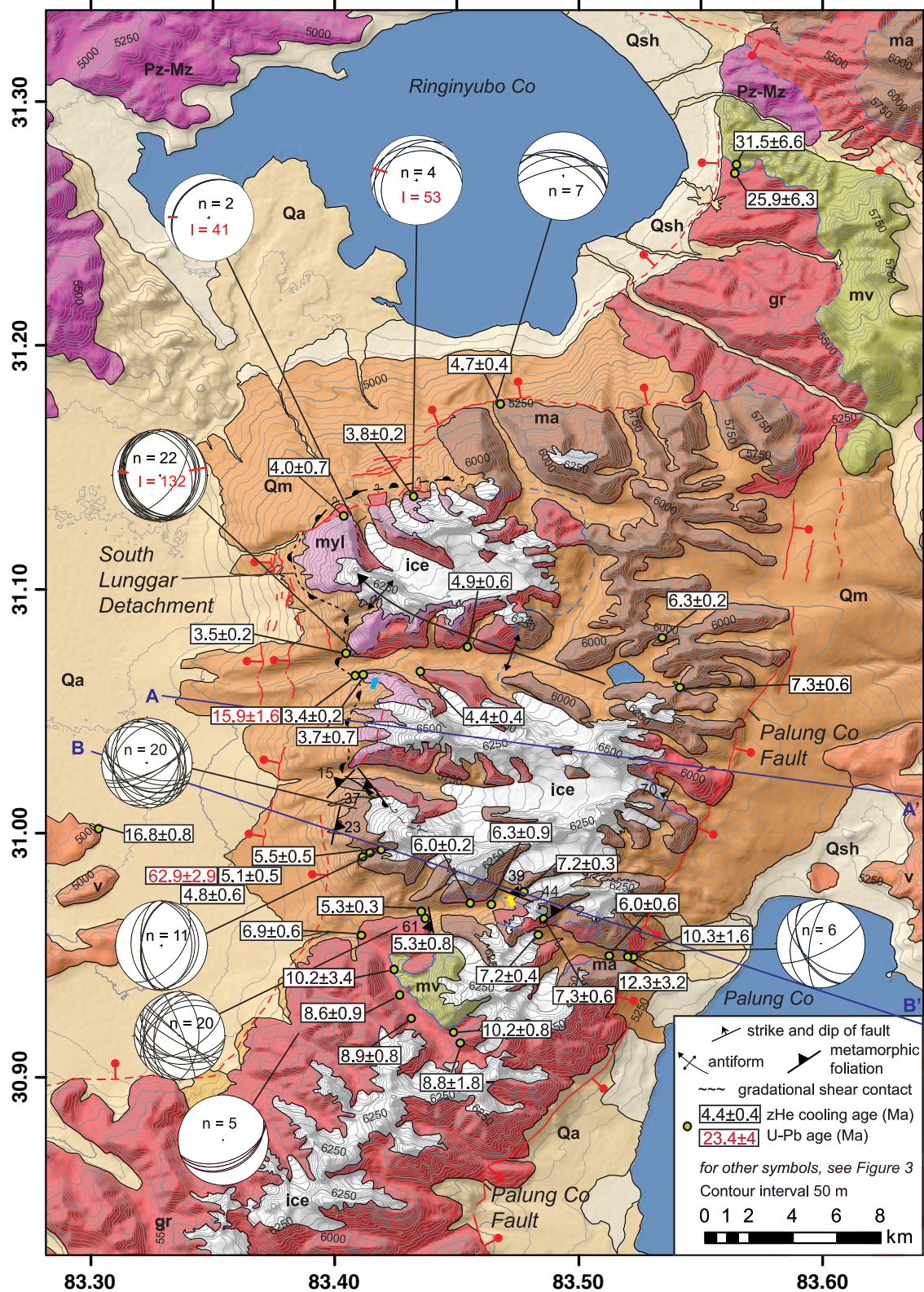


**Figure 4.** Geologic map of the South Lunggar rift. See Figure 3 for location. Note that cross-section lines A-A' and B-B' extend off the map to the east; see Figure 3 for full extent. On stereonets, “n” indicates the number of fault planes plotted, and “l” indicates the number of fault striations or stretching lineations measured; red lines indicate average orientation of lineations. Small blue and yellow arrows indicate position and direction field photographs (Figures 5c and 6c) were taken at. Zircon (U-Th)/He mean and  $1\sigma$  errors are shown as well. Note the age for collocated samples SLE-SCTR-01 and SLE-SCTR-02 ( $30.94907^\circ\text{N}$ ,  $83.52237^\circ\text{E}$ ) is the mean age for all aliquots.

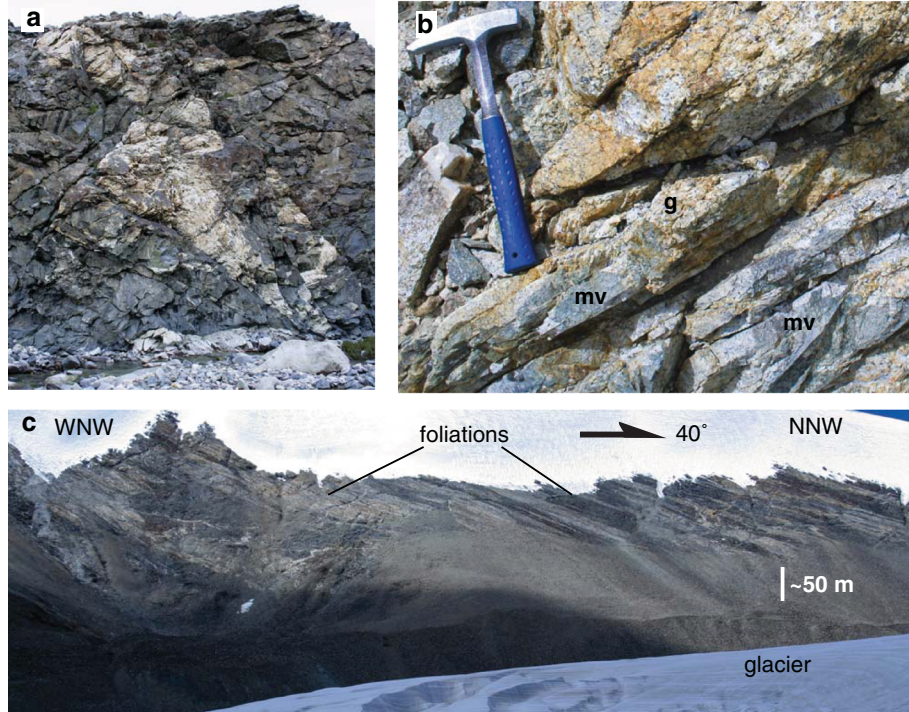


**Figure 5.** Field relationships in the southern Surla Range. (a) Undefomed leucogranites intruding pervasively fractured amphibolite. Outcrop is approximately 3 m tall. (b) Leucogranite intruding greenschist-facies metavolcanic rocks. (c): Northwest looking view of moderately north-dipping gneissic foliation above glacier. Photograph taken from location and orientation indicated by yellow arrow in Figure 4; direction of view is perpendicular to arrow with trend shown.

greenschist-facies volcanic rocks (**mv**) intruded by variably deformed leucogranites (**gr**, **myl**). Hanging-wall rocks on both sides of the rift include unmetamorphosed volcanic rocks (**v**) and sedimentary rocks composing a Cretaceous thin-skinned thrust belt (**K**) (Figures 3 and 4). In general, ice and moraine cover and extensive talus development limited access to bedrock exposure, inhibiting more extensive sampling, measurement of structural data, and contact identification, although high walls of glacial valleys and sporadic outcrop allowed for confident mapping of rock units.

[21] The amphibolite-grade metamorphic unit (**ma**) is a composite unit of different rock types, mapped as one unit. The unit is composed of coarse-grained biotite amphibolite, biotite granite orthogneiss, and biotite granodiorite orthogneiss. The orthogneiss is locally migmatitic. Contacts between the different subunits were not observed, and relationships are uncertain. Foliations in the orthogneiss are strongly developed with individual bands mm to 10s of meters in thickness. Amphibolites are unfoliated to moderately foliated at the hand sample to meter scale, and a well-developed foliation is visible in glacier-polished valley walls (Figure 5c). The foliation is generally north dipping, though significant variability exists (Figure 4), and therefore the metamorphic event that deformed these rocks is interpreted to be unrelated to the modern phase of extensional deformation. This interpretation is supported by the widespread intrusion of undefomed leucogranite (described below). No ductile stretching fabrics or other lineations were observed in outcrop, although they were occasionally spotted in talus or glacial debris. Leucogranite intrusion is widespread

and locally preferentially occurs along foliation planes (Figure 5c). Lower-grade (greenschist-facies) felsic to intermediate fine-grained metavolcanic rocks (**mv**) are present in two major areas (Figure 4) and in small lenses (below map resolution) on the northern margin of the range. Biotite displays kink banding and alteration to chlorite, indicative of greenschist-facies metamorphism. These rocks are observed to be intruded by granites, though the nature of contact between higher-grade metamorphic rocks was not observed. The unit may correlate to the Burial Hill volcanic rocks mapped by *Murphy et al.* [1997] along strike ~150 km to the east.

[22] Biotite leucogranite intrusions (**gr**) are widespread, from meter to up to 10s of km scales (Figures 4 and 5c). These intrusions are observed in the metamorphic units (**ma**, **mv**) (Figures 5a and 5b). U-Pb ages (section 4) indicate both Gangdese (~65 Ma) and early- to mid-Miocene (22–16 Ma) crystallization ages, although there are no significant petrologic differences between rocks of different ages. Therefore, the large leucogranite bodies may be made up of smaller plutons that intruded episodically over 10s of m.y. In the northwestern Surla Range, structurally below the South Lunggar detachment (SLD), the leucogranite is heavily sheared into a mylonitic zone (**myl**). No garnet or other mineral phases indicative of intrusion or deformation at high pressures are present in the leucogranites.

[23] Hanging-wall rocks consist of a Cretaceous thrust belt of Paleozoic and Mesozoic supracrustal rocks (**K**) [*Murphy et al.*, 1997] and unmetamorphosed biotite-and hornblende-bearing felsic volcanic rocks (**v**). These volcanic rocks have

**Table 1.** Zircon (U-Th)/He Sample Summary<sup>a</sup>

Sample	Mean (Ma)	St. Dev. (Ma)	Age Err. (Ma)	Latitude (°)	Longitude (°)	Altitude (m)
SLE-NMT-02	7.3	0.6	0.6	31.05958	83.54151	5823
SLE-NMT-03	6.3	0.2	0.5	31.08004	83.5342	6063
SLE-SCTR-01	9.4	0.8	0.7	30.94907	83.52237	5366
SLE-SCTR-02	11.8	1.5	0.9	30.94907	83.52237	5366
SLE-SCTR-03	12.3	3.2	1.0	30.94915	83.52008	5604
SLE-SCTR-05	6.0	0.6	0.5	30.94966	83.51246	5477
SLE-SCTR-06	7.2	0.4	0.6	30.95814	83.48333	5826
SLE-SCTR-07	7.3	0.6	0.6	30.96490	83.48569	5979
SLW-BSTR-01	10.2	3.4	0.8	30.94404	83.42437	5450
SLW-BSTR-02	8.6	0.9	0.7	30.93364	83.42674	5478
SLW-BSTR-03	8.9	0.8	0.7	30.92383	83.43140	5641
SLW-BSTR-05	8.8	1.8	0.7	30.91829	83.44883	5873
SLW-BSTR-06a	10.2	0.8	0.8	30.91379	83.45148	5874
SLW-CCTR-03	5.3	0.8	0.4	30.96502	83.43724	5622
SLW-CCTR-04	5.3	0.3	0.4	30.96790	83.43554	5490
SLW-CCTR-05	6.0	0.2	0.5	30.97127	83.45555	5663
SLW-CCTR-06	6.3	0.9	0.5	30.97082	83.46420	5719
SLW-CCTR-07	7.2	0.3	0.6	30.97590	83.47744	5848
SLW-HW-01	16.8	0.8	1.3	31.00171	83.30310	4960
SLW-LK-01	25.9	6.3	2.1	31.27406	83.56464	5010
SLW-LK-02	31.5	6.6	2.5	31.27406	83.56464	5010
SLW-NC-02	4.8	0.4	0.4	31.17597	83.46808	5201
SLW-NFT-01	3.8	0.2	0.3	31.13807	83.43247	5811
SLW-NMT-01	3.5	0.2	0.3	31.07366	83.40467	5381
SLW-NMT-02	3.4	0.2	0.3	31.07363	83.40496	5416
SLW-NMT-03	3.7	0.7	0.3	31.06495	83.41171	5538
SLW-NMT-04	4.4	0.4	0.4	31.06623	83.43498	5609
SLW-NMT-05	4.9	0.6	0.4	31.07644	83.4545	5628
SLW-NWC-01	4.0	0.7	0.3	31.13001	83.40368	5701
SLW-SFTR-01	4.8	0.6	0.4	30.99023	83.41145	5676
SLW-SFTR-02	5.1	0.5	0.4	30.99191	83.41448	5724
SLW-SFTR-04	5.5	0.5	0.4	30.99297	83.41912	5810
SLW-STR-01	6.9	0.6	0.6	30.95806	83.41096	5275

<sup>a</sup>Individual aliquot analyses shown in the supporting information (Table S2). Age error is 8% 2σ laboratory analytical error (see text for discussion).

a middle Miocene zHe cooling age ( $16.8 \pm 0.8$  Ma; Figure 4 and Table 1), interpreted as an eruption age due to the vesicular texture suggesting little to no postdeposition burial and reheating. The presence of hornblende, not found in the leucogranites, suggests an eruptive source external to the Surla Range.

## 2.2. Quaternary Units

[24] Quaternary sedimentary units are dominantly the products of erosion of the Surla Range massif and include two generations of Quaternary alluvium (**Qa** and **Qo**), Quaternary moraine and outwash (**Qm**) and Quaternary shorelines (**Qsh**). **Qo** is the older Quaternary unit, cut off from modern depositional systems by uplift or drainage reorganization. **Qa** is found in active to recently active depositional environments. The age of **Qm** is unknown, but it is reworked by the highest shorelines (**Qsh**), which are dated at the nearby Ngangla Ringco (Figure 3) at ~10.4 ka (A.M. Hudson, electronic personal communication, 2012).

## 3. Structural Geology of the SLR

[25] The Surla Range is uplifted on its eastern flank by a moderately east-dipping normal fault, here named the Palung Co fault, and on its northwestern side by a low-angle west-dipping normal fault, here named the SLD, which is linked with moderate to high-angle west-dipping normal

faults on the northwestern and southwestern margins of the Surla Range.

### 3.1. Palung Co Fault

[26] The Palung Co fault is a moderate-angle east-dipping normal fault striking  $20^\circ$  in the north and  $350^\circ$  in the south (Figure 3). The fault is ~80 km along strike and cuts into the Gangdese (Transhimalaya) Range south of the Surla Range. Where it bounds the Surla Range, it forms  $40^\circ$ – $50^\circ$  east-dipping triangular facets up to 1 km high. A lake, Palung Co, occupies much of the ~10 km wide rift basin east of the fault trace (Figure 4). The fault has uplifted leucogranites and amphibolites in the footwall 1.5 km above the sedimentary and volcanic rocks in the hanging wall, giving a minimum amount of throw of 1.5 km; however, the estimated sedimentary and volcanic cover thickness of ~8 km [Murphy et al., 1997; 2010] and young zircon (U-Th)/He cooling ages (section 5) suggests throw on the fault may be greater. Interpretation of rift morphology [e.g., Friedmann and Burbank, 1995] and thermochronology suggests that the area near Palung Co is the zone of maximum fault displacement. The Palung Co fault is currently active, as indicated by small fault scarps in ground moraine visible in remote sensing imagery near the fault's northern tip (Figure 4). Additionally, in August 2008, a series of earthquakes occurred along the fault. The largest was a  $M_w$  6.7 normal faulting event [Elliott et al., 2010; Ryder et al., 2012]. Body wave seismology and synthetic aperture radar

interferometry (InSAR) indicate the rupture occurred on two fault planes, one projecting directly to the rangefront fault in the study area and the other several km to the south [Elliott *et al.*, 2010]. Those authors estimated the northern rupture to be striking  $20^\circ$  and dipping  $43 \pm 2^\circ$  E, in very close agreement with our field observations. Their modeling suggests that the top of the northern rupture patch was 2–5 km deep, and the bottom was 14–20 km deep. The shallow termination of seismic slip and InSAR phase continuity across the fault trace [Elliott *et al.*, 2010; Ryder *et al.*, 2012] is consistent with our observations from mapping the area 12 months after the event indicating no obvious surface rupture. The southern rupture is roughly along strike of the northern rupture, but is south of a change in the mapped fault strike and cuts into the high topography in the Surla Range or Gangdese Range (the two ranges merge at this latitude), and has no clear geomorphic expression [Elliott *et al.*, 2010]. This difference in strike between the rangefront and the rupture possibly represents the southward propagation of the northern Palung Co fault and cessation of activity on the previous southern segment to the east, consistent with models of developing normal fault systems that hypothesize the simplification and organization of rift geometry into one relatively planar master fault through time [e.g., Bosworth, 1985].

### 3.2. SLD

[27] The northwestern portion of the Surla Range is uplifted along the SLD. The SLD is a shallowly north- to west-dipping normal fault that is interpreted to link at depth with the steeper range-bounding normal faults to the north (Figure 3); however, thick moraine cover obscures the fault linkage at the surface, though possible fault scarps in moraine suggest partitioning of normal and strike-slip motion into two main strands (Figure 4). To the south, it is linked with a moderate-angle normal fault (section 3.3), though we restrict the use of the name “SLD” to the northern fault. In its footwall, the SLD has exhumed leucogranite and amphibolite. In places on the western rangefront, triangular facets dipping  $\sim 20^\circ$  W are preserved (Figure 7), though extensive glaciation has modified the rangefront elsewhere. Except in its southern extent, hanging-wall rocks are not observed near the trace of the SLD due to thick moraine cover, and the fault is not observed in bedrock.

[28] Immediately below the detachment, footwall leucogranites display a mylonitic shear zone  $>100$  m thick. Foliation planes in the mylonites strike parallel to the local trend of the rangefront, and where measured (at lower elevations) dip  $\sim 20^\circ$ , though the shear zone is observed to flatten out to  $<10^\circ$  at the crest of the range (Figure 6c). Lineations, defined dominantly by ribbons of quartz, are consistently oriented WNW with much less variance than the strike of the foliations (Figure 4); slip on the northern part of the SLD is highly oblique (see kinematic data on Figure 4). Kinematic indicators such as S-C fabrics, sigma and delta clasts indicate a top down to the west, normal sense of shear (Figures 6a and 6b). Large feldspar crystals show brittle deformation instead of ductile deformation, indicating that mylonitization was not entirely in the ductile regime as might be expected if the shear zone formed during magma emplacement. The mylonitic shear zone is therefore interpreted to be the exhumed downdip extension of SLD shear in the brittle-ductile transition zone. The orientation

of foliations broadly defines an antiform that we suggest is a single corrugation of the detachment footwall, with the antiformal axis trending in the direction of extension (Figure 4). This configuration is similar to analogous structures well defined in the Basin and Range extensional province of the western US [e.g., Duebendorfer *et al.*, 2010; John, 1987], as well as in metamorphic core complexes worldwide [e.g., Spencer, 2010].

[29] Brittle structures in the SLD footwall consist of chatter marks on the west- to north-dipping foliation planes, with steps consistent with top-W (normal sense) displacement. East-dipping low-angle normal faults with mm to cm scale offsets were also observed; these are interpreted to be products of flexural rotation of the footwall through the upper (antilistric) part of a rolling hinge [e.g., Buck, 1988; Axen and Bartley, 1997]. This interpretation is supported by the observed shallowing of the mylonitic shear zone at the crest of the Surla Range, and by (U-Th)/He data and thermokinematic modeling (section 5).

[30] Though no seismic events on the SLD are represented in global catalogs, it is believed to have been recently active due to well-developed fault scarps along its trace (Figures 3 and 7). The largest fault scarps associated with the SLD are 2 and 3 km basinward of the rangefront (Figure 4). These two west-dipping fault scarps cut a large lateral moraine extending into the basin and have a cumulative  $\sim 112$  m of down-to-the-west throw, as determined by Jacob staff field measurements. These faults are considered to sole into the SLD at depth; observations of much smaller scarps at the SLD's trace at the rangefront immediately east imply that the SLD is active and uncut by the faults in its hanging wall. This arrangement of faults is similar to that observed in the NLR [Kapp *et al.*, 2008], although in the NLR, the detachment is inactive at the range front; the important point is that the dominant neotectonic expression of faulting has migrated away from the rangefront, but slip is interpreted to occur along the detachment at depth. The dissection of the detachment hanging wall by high-angle normal faults is a very common feature of low-angle normal fault systems in the Basin and Range and may be a consequence of isostatic uplift of the footwall following tectonic exhumation [Kapp *et al.*, 2008], and possibly as part of an evolving rolling-hinge detachment system [e.g., Axen and Bartley, 1997].

[31] The structure of the northern Surla Range, where bounded by the SLD, is shown in a cross section across the range (Figure 8a). The observed gently antilistric geometry of the detachment fault and underlying shear zone are continued at depth. The maximum amount of possible extension in the SLR can be estimated by the horizontal distance between preextensional strata in the hanging walls. This distance is  $\sim 20$  km at the latitude of the section, although it increases northward. This estimate is dependent on the depth of the flanking rift basins, which is unconstrained; the deeper the basins, the greater the distance between the prerift hanging-wall strata. By limiting basin depth to less than 1 km, consistent with observations of other supradetachment basins [Cogan *et al.*, 1998; Friedmann and Burbank, 1995], we obtain a lower-bound estimate for maximum extension (deeper basins would move the hanging-wall pinning points farther away from each other, which would increase the possible maximum extension). It is important to note that the estimate of maximum extension is only influenced by

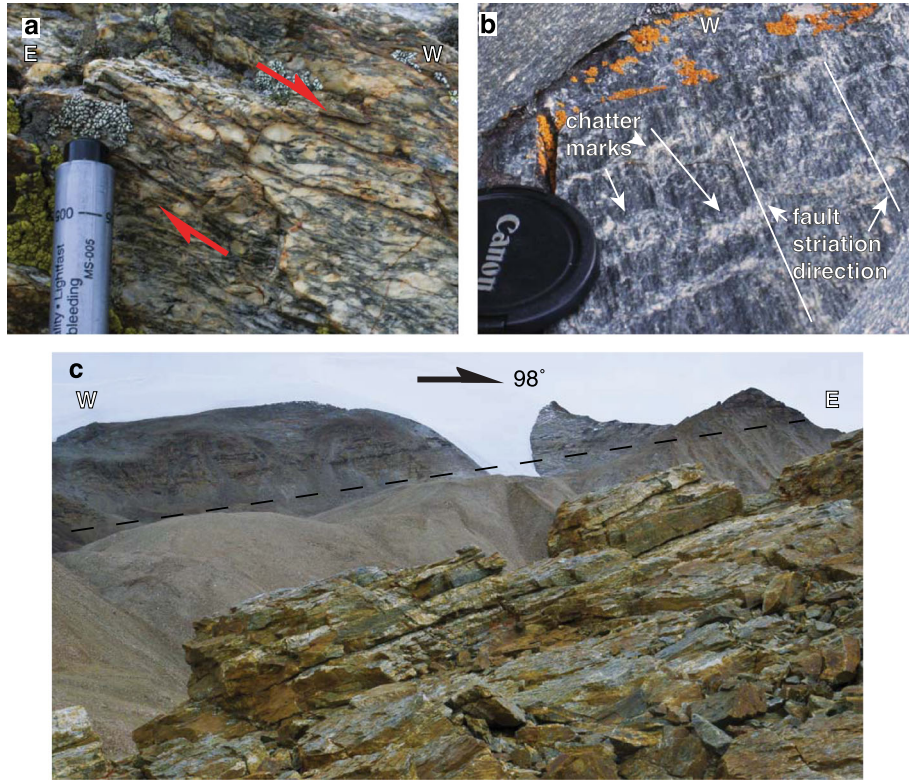


**Figure 6.** Field photographs of mylonitic shear zone near the detachment fault trace. (a) Close-up of mylonitic fabric showing interpreted normal shear sense. View is to the south. (b) View W (in interpreted direction of slip) of parallel fault striations and stretching lineations, as well as chatters indicating normal-sense brittle slip along the mylonitic foliation planes. (c) North-northeast looking view of gently west-dipping mylonitic gneiss in foreground, and foliated rocks interpreted to be continuation of shear zone on the ridgeline in the background. Dashed line indicates bottom of mylonitic foliation; leucogranites below are essentially undeformed. Photograph taken from location and orientation indicated by blue arrow in Figure 4; direction of view is perpendicular to arrow with trend shown.

plausible fault geometries in a small way, as can be envisioned by examining the cross section (Figure 8a). If the faults were vertically dipping, the hanging-wall pinning points would be  $<5$  km closer to each other; conversely, if the faults were very shallowly dipping (both  $<20^\circ$ ), the maximum extension would be  $<5$  km greater.

[32] ZHe ages young westward, suggesting that the SLD has accommodated significantly more exhumation (and therefore extension) than the Palung Co fault at this latitude.

This requires top-east horizontal-axis rotation of the Surla Range away from the detachment fault as has been suggested for detachment footwalls elsewhere in Tibet [e.g., Kapp *et al.*, 2005a; Kapp *et al.*, 2008] and worldwide [e.g., Buck, 1988]. This is discussed in more detail in section 5.

### 3.3. Moderate-Angle Normal Fault

[33] To the south of the SLD, uplift of the Surla Range is accommodated by a moderate to high-angle normal fault.

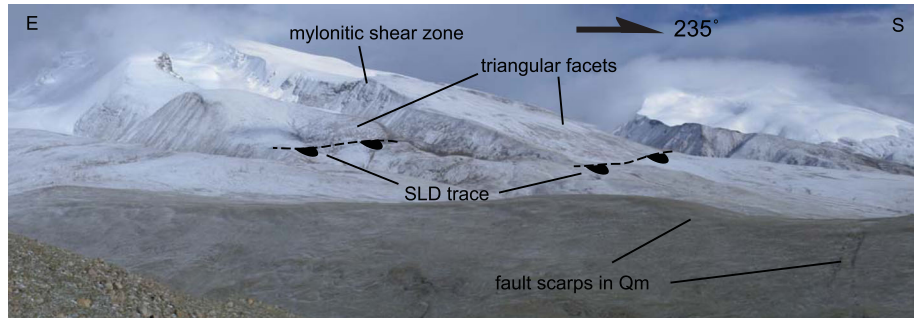


**Figure 7.** Southeast looking view of Surla Range showing triangular facets and mylonitic shear zone above the approximate trace of the SLD (here buried under  $Q_m$ ), as well as normal fault scarps (with different degrees of weathering) in Quaternary moraine extending past the rangefront. Direction of view is perpendicular to arrow with trend shown.

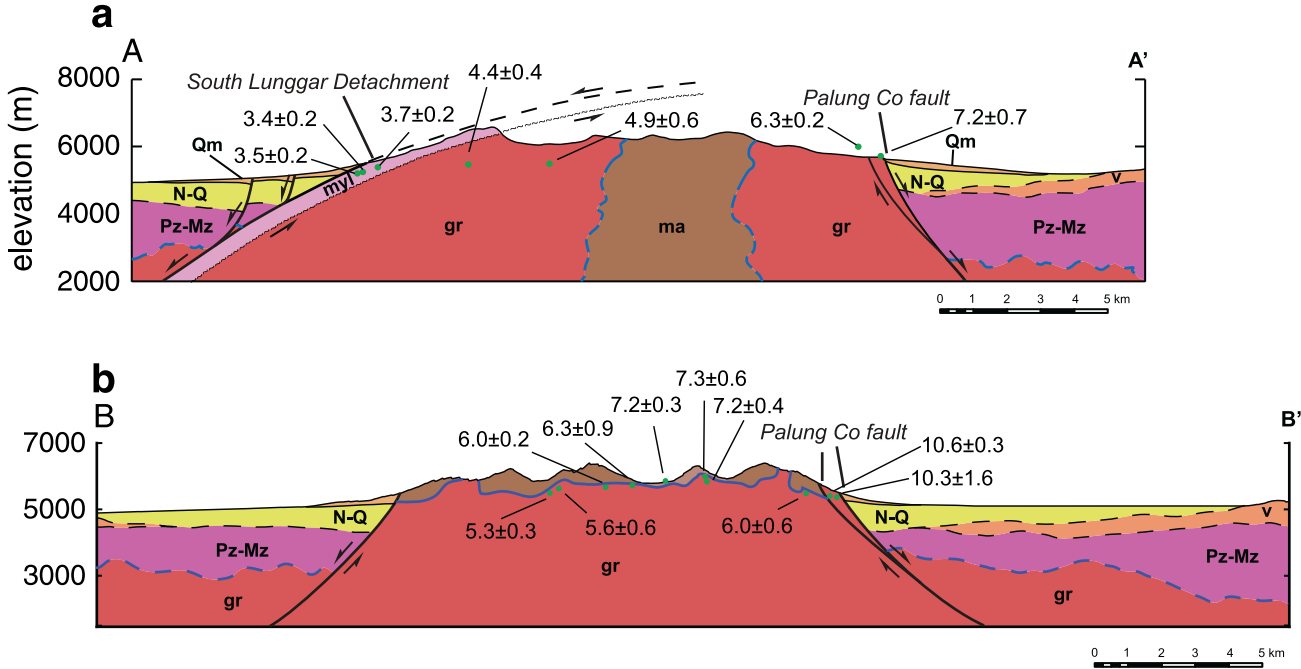


**Figure 8.** (a) Structural cross section through the northern transect of the SLS (A-A' on Figure 4) showing low-angle South Lunggar Detachment and moderate-angle Palung Co fault. (b) Structural cross section through the southern transect of the SLS (B-B' on Figure 4) showing moderately dipping faults bounding the range.

The fault changes strike from NNE in the north, near the SLD, to E-W in the south as it wraps around west to bound the southern margin of the western SLR basin (Figure 3). Though the fault is not exposed, subordinate high-angle (~55°) west-dipping small-displacement faults in the footwall are likely parallel to the master fault. The rangefront of the Surla Range becomes significantly steeper south of the SLD as well. Quaternary fault scarps on the range-bounding fault were not definitively observed in the field. Cross section B-B' (Figure 8b) characterizes the southern part of the Surla Range. Maximum extension across this section is ~16 km, with the same assumptions and caveats as the northern cross section. As discussed in more detail in sections 5 and 6, zHe data and thermokinematic modeling suggest that at this latitude, both the west-dipping and east-dipping (Palung Co fault) structures have accommodated similar amounts of exhumation, and little to no horizontal-axis rotation of the Surla Range has occurred.

### 3.4. Interior Structures of the Surla Range

[34] No major structures were mapped within the interior of the Surla Range; however, fault surfaces were found in almost every outcrop in the southern Surla Range, where older rocks were more exposed and accessible. These dominantly strike roughly E-W, although some high-angle N-striking fault surfaces were observed (Figure 4). No evidence was found for a shallowly west-dipping fabric that could have been reactivated during extension and influenced detachment fault geometry.

[35] A well-developed foliation, with planes meters to 10s of meters thick, dips northward moderately to gently (Figure 5c); in places, it is unclear if this fabric is a true metamorphic foliation or if it is an intrusive complex, with younger leucosomes intruding older mafic and felsic rocks

(possibly along a preexisting fabric). In most locations, no foliation was observed in the mafic rocks (mostly amphibolites) at the outcrop scale, although they were generally more pervasively faulted. This may indicate that metamorphism occurred at relatively low temperatures, and the amphibolites deformed brittlely while the felsic orthogneisses deformed ductilely. Alternatively, this could indicate that the mafic rocks are younger than the foliation event; these may be basalt dikes that were subsequently metamorphosed to amphibolite facies under low differential stress.

### 3.5. Accommodation Zone

[36] E-W striking brittle faults bound the northern side of the northwestern Surla Range. Though we found no fault striations on the northern brittle faults that would indicate the rake of slip, the faults are probably oblique slip (normal and left-lateral), given their orientation relative to that of the strain field in the region and throughout Tibet, which is undergoing ~N-S contraction. This would give them similar kinematics to that observed in the mylonites several km to the west along strike. It is likely that these faults serve to relieve stresses related to significant differential exhumation of the Surla Range to the south and less-exhumed rocks to the north. The northern Surla Range decreases in elevation to the north, into the accommodation zone between the NLR and SLR. The Palung Co fault and the North Lunggar detachment (NLD) tip out on the east side of the range here, and uplift is only accommodated on the western fault, which runs north from the SLD to the southern North Lunggar Shan. ZHe cooling ages are Oligocene for rocks in the footwall of this western fault, indicating limited exhumation (see section 5). Steep topographic breaks and exhumation of granites and gneisses juxtaposed against lower grade rocks suggest that significant normal faulting exists within this zone in addition

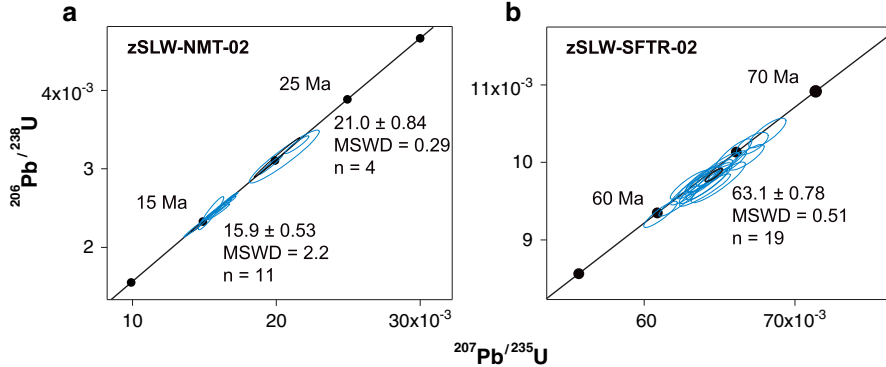


**Figure 9.** Concordia plots of zircon U-Pb ICP-MS rim analyses of two samples showing weighted mean  $^{238}\text{U}/^{206}\text{U}$  ages. (a) Sample zSLW-NMT-02, mylonitized leucogranite from mylonite zone near SLD trace. Best fit ellipse shown in black, with individual grain analyses shown in blue. Two populations are visible, one at  $\sim 15.9$  Ma and one at  $\sim 21.0$  Ma. (b) Sample zSLW-SFTR-02, ductilely deformed leucogranite from SLR footwall. Ages cluster at  $\sim 63$  Ma, indicating Gangdese-age magmatism. See Figure 4 for sample locations.

to the rangefront faults (Figures 3 and 4), although this area was not mapped in detail.

#### 4. Zircon U-Pb Geochronology

[37] Zircons from a mylonite sample (SLW-NMT-02) from the SLD shear zone and a mildly deformed leucogranite sample (SLW-SFTR-02) were dated by the U-Pb method with laser ablation inductively coupled plasma mass spectrometry (LA-ICP-MS) in order to bracket the timing of magmatism and place age constraints on other map units and geologic events through cross-cutting relationships. Two samples were selected because they both display evidence of ductile deformation and have Pliocene zHe cooling ages, raising the possibility that ductile deformation was syn-kinematic, and that cooling ages may be young because of residual heat from magmatism. The first possibility is relevant because it may indicate that observed mylonitization may be a result of intrusive processes instead of detachment faulting [e.g., Daoudene *et al.*, 2012], challenging our interpretation of the northern Surla Range as a metamorphic core complex. The second possibility is relevant because residual heat from magmatism would invalidate the assumption of cooling due to exhumation, rendering our thermochronologic interpretations inaccurate. Alternately, if these leucogranites are very old, the observed ductile deformation may be due to a previous deformational episode involving  $\sim$ E-W extension, also challenging our core-complex interpretation.

#### 4.1. Methods

[38] U-Pb ages were determined by LA-ICP-MS using a Thermo Scientific Element 2 ICP/MS at the University of Kansas. A Photon Machines 193 nm ArF excimer laser was used to ablate  $29\ \mu\text{m}$  spots on whole zircon crystals placed on double-sided tape. The laser was set to  $3.5\ \text{J cm}^{-2}$  fluency at 10 Hz repetition rate, which produced ablation pits of  $\sim 20\ \mu\text{m}$  depth, with the ablated material carried to the ICP/MS in He gas with a flow rate of  $0.74\ \text{L min}^{-1}$ , tied in with Ar gas at  $1.0\ \text{L min}^{-1}$  flow rate with a Y-connector 15 cm down flow from the ablation cell. Elemental fractionation, downhole fractionation, and calibration drift were corrected

by bracketing measurements of unknowns with GJ1 zircon reference material [Jackson *et al.*, 2004] and data reduction using the VisualAge data reduction scheme [Petrus and Kamber, 2012] for the IOLITE software package [Paton *et al.*, 2011]. Because the zircon crystals were not polished, multiple growth zones were ablated during some analyses. Ages were calculated only for the outermost growth zones (rims) in these cases. Within run, reproducibility of the GJ1 reference material [Jackson *et al.*, 2004] was better than 2% on the U-Pb age. Results were corrected for diffusive lead loss and common lead with the methods of Andersen [2002].

#### 4.2. Results

[39] Results are shown in Figure 9 and Data Table S1. Python code to calculate statistics is given in the supporting information (calculate\_weighted\_means.py and geochron\_stats.py). Sample SLW-SFTR-02 (Figure 9a) has a  $^{238}\text{U}/^{206}\text{U}$  weighted mean age of  $63.1 \pm 0.78$  Ma (95% confidence:  $2\sigma/\sqrt{n}$ ,  $n = 19$ , MSWD = 0.51). This suggests it is related to Gangdese magmatism, as the sample is  $\sim 20$  km from the northern margin of the Gangdese range. Zircons from sample SLW-NMT-02 (Figure 9b) display evidence of zoning (major, step-wise changes in isotopic ratios during laser ablation) and yield early Miocene rim ages, with a  $^{238}\text{U}/^{206}\text{U}$  weighted mean age of  $16.2 \pm 0.77$  Ma ( $n = 15$ , MSWD = 2.0). The sample also shows two populations of rim ages, a dominant group ( $n = 11$ ) with a  $^{238}\text{U}/^{206}\text{U}$  weighted mean age of  $15.9 \pm 0.53$  Ma (MSWD = 2.2) and a lesser one ( $n = 4$ ) of  $21.0 \pm 0.84$  (MSWD = 0.29). These crystallization ages are  $\sim 58$  and  $\sim 12$ – $17$  Ma older than the zHe ages for each sample ( $5.1 \pm 0.5$  Ma and  $3.4 \pm 0.2$  Ma, respectively; section 5, Table 1), confirming that Pliocene cooling age for sample SLW-SFTR-02 is not likely to be the result of residual magmatic heat. It is possible that some residual magmatic heat could influence the zHe age of sample SLW-NMT-02, although this effect is likely small, because the zHe age is only  $\sim 1.5$  m.y. younger than the zHe age from the Paleocene granites to the south, and is from an area that appears to be exhumed more rapidly based on the much larger Quaternary fault scarps and localization of extension on the SLD at that latitude. Additionally,

though SLW-NMT-02 displays evidence of zoning, U and Th concentrations are not systematically higher in the rims than in the cores of the zircons, indicating that the (U-Th)/He ages are not influenced by compositional zoning of parent isotopes.

[40] Given that the fabrics in both the Paleocene and early Miocene leucogranites are indicative of ~E-W extension, which has not been documented in southern Tibet before the middle Miocene, these fabrics are likely the result of Neogene extensional processes and unrelated to magmatic processes. This is supported by the observation that feldspars within the mylonitic shear zone show only slight evidence for ductile deformation and pervasive brittle deformation, suggesting that mylonitization took place at cooler temperatures than would be expected for syn-intrusive deformation (see *Daoudene et al.* [2012] for the converse case).

## 5. Zircon (U-Th)/He Thermochronology

[41] In order to understand the history of deformation in the SLR in a quantitative fashion, we used zircon (U-Th)/He, or zHe, thermochronometry. This is a technique that utilizes the temperature-dependent diffusion of radiogenic  $^{4}\text{He}$  out of a mineral grain to understand the cooling history of that grain. More specifically, it quantifies the time since a mineral grain cooled through a temperature range that is a function of the diffusion parameters for that type of mineral and the cooling rate, approximated by a “closure temperature” [Dodson, 1973]. For rapidly cooled zircons (e.g., cooling rates of  $20\text{--}100^{\circ}\text{C Ma}^{-1}$ ), this closure temperature is  $\sim 190\text{--}200^{\circ}\text{C}$  [Reiners, 2005]. The thermal sensitivity window (defined as a temperature range) yields a depth range termed the “partial retention zone” via the geothermal gradient. Below the partial retention zone, radiogenic  $^{4}\text{He}$  is diffused out of the grain as fast as it is produced, while above this zone, diffusion is extremely slow.

[42] The temperature and depth sensitivity of zHe thermochronometry is ideal for studying rifts with significant amounts of footwall exhumation, because the partial retention zone is deep enough to be less sensitive to surface processes such as erosion and hydrothermal circulation than for lower temperature thermochronometers such as apatite, while still being shallow enough to be responsive to tectonic exhumation [Reiners, 2005].

[43] We have collected samples from throughout the Surla Range, with emphasis on two transects across the range near the cross sections A-A' and B-B'. These transects are analyzed through 3-D thermokinematic modeling in order to place quantitative estimates on the deformational history, and the other samples (spanning a more broad geographical range) are interpreted in a less quantitative fashion.

### 5.1. Zircon (U-Th)/He Results

[44] Zircons from 33 samples (two to six single-grain aliquots per sample) were run for (U-Th)/He analysis at the University of Kansas Isotope Geochemistry Laboratory following procedures described by *Wolfe and Stockli* [2010]. Individual aliquot outliers were rejected according to Peirce's criterion [Ross, 2003]. Mean sample results are shown in Table 1, and individual aliquot results are shown in Table DR2. The cooling ages of all samples in the Surla Range are late Miocene to Pliocene (Figure 4 and Table 1),

indicating that late Miocene to present exhumation for the entire range has been greater than the depth of the preextensional zircon He partial retention zone, i.e.,  $>5\text{--}10\text{ km}$  for mean geothermal gradients of  $40\text{--}20^{\circ}\text{C km}^{-1}$ . In general, ages increase both with elevation and with distance from the SLD. For the northern sampling transect, corresponding to cross section A-A' (Figures 4 and 8a), cooling ages decrease monotonically from  $7.3 \pm 0.6$  ( $1\sigma$ ) in the east to  $3.4 \pm 0.2$  in the west, at the SLD trace. This cooling pattern suggests that cooling has been accommodated by progressive exhumation and top-to-the-east rotation of the SLD footwall. For the southern sampling transect (Figures 4 and 8b), cooling ages decrease from  $7.3 \pm 0.6$  for the highest sample, in the center of the range, downhill, and to the east and west. Age-elevation relationships are generally similar for both sides of the Surla Range, though there are more samples on the west side. This pattern suggests relatively vertical uplift of the Surla Range at this latitude, accommodated equally on both range-bounding faults. The eastern range-bounding fault, the PCF, has a step over between two fault strands where this sampling transect crosses it. Samples from in between the two fault strands show  $10\text{--}12\text{ Ma}$  cooling ages (Figure 4), suggesting that the tectonic sliver in between the fault strands was not exhumed as much or as rapidly as the main Surla Range.

[45] Cooling ages older than late Miocene are found in two locations: an age of  $16.8 \pm 0.8\text{ Ma}$  for a tuff (unit v) in the western rift basin, which is interpreted to be the depositional age of the tuff, as its brittle, vesicular texture is not indicative of deep burial. A metavolcanic rock (mv) in the footwall of the accommodation zone between the NLR and SLR and a leucogranite (gr) that intrudes it yielded cooling ages of  $32 \pm 7\text{ Ma}$ ,  $26 \pm 6\text{ Ma}$ . These samples are interpreted as being within in or above the mid-Miocene (preextensional) zircon He partial retention zone, which limits late Miocene to present exhumation of the accommodation zone to be less than  $\sim 5\text{--}10\text{ km}$ .

### 5.2. Thermal Modeling With Pecube

[46] Although the data provide a reasonable first-order picture of relative exhumation rates and some information on timing, they do not directly provide the fault slip rates or precisely estimate the timing of rift initiation in the SLR. While some of this information can be obtained through analysis of (U-Th)/He age-elevation or age-fault distance relationships [e.g., *Stockli*, 2005], complications relating to the dynamic thermal (e.g., unknown or transient geothermal gradient, radiogenic heating) and structural (e.g., footwall rotation) state of the extending crust can introduce inaccuracies to such estimates [*Stockli*, 2005; *Robinson et al.*, 2010; *Ehlers*, 2005]. We have therefore chosen to analyze our data with the thermochronological modeling code Pecube [*Braun*, 2003; *Braun et al.*, 2012]. Pecube uses the finite element method to iteratively solve the 3-D heat transport equation throughout an imposed tectonogeomorphic scenario and is able to incorporate these aforementioned parameters that affect thermochronometric ages. In order to robustly constrain the Miocene to present deformational history of the SLR, we perform an iterative grid search throughout the parameter space characterizing deformational history, constrained by structural data, and then accept the deformational histories that fit the zHe cooling ages within a 95% confidence limit, to quantify the deformation history and uncertainty of the SLR.

**Table 2.** Parameters for Models Setup, and Rates and Timing of Faulting for Pecube Modeling of the North and South zHe Sampling Transects<sup>a</sup>

Thermal and Grid Parameters	Value	Unit	
Model depth	80 + elev (a.s.l.)	km	
North Transect length, width	98 E-W, 4.9 N-S	km	
South Transect length, width	93 E-W, 4.2 N-S	km	
FEM node spacing (horizontal, vertical)	0.785, 3.55	km	
Thermal diffusivity	25	$\text{km}^2 \text{Ma}^{-1}$	
Radiogenic heat production	20	$^\circ\text{C Ma}^{-1}$	
Moho temperature	1200	$^\circ\text{C}$	
Surface temperature	0	$^\circ\text{C}$	
Atmospheric lapse rate	0	$^\circ\text{C km}^{-1}$	
<i>North Transect fault parameter</i>			
SLD initiation	Range 8 – 18	Step 1	Unit Ma
SLD initial slip rate	0.25 – 3.0	0.25 – 0.5	$\text{mm a}^{-1}$
SLD acceleration	2 – 6.5	0.5	Ma
SLD postacceleration slip rate	1.5 – 4.5	0.5	$\text{mm a}^{-1}$
PCF initiation	10 – 18	2	Ma
PCF slip rate	0.25 – 1.5	0.25 – 0.5	$\text{mm a}^{-1}$
<i>South Transect fault parameter</i>			
PCF initiation	10 – 18	2	Ma
PCF initial slip rate	0.5 – 2.0	0.5 – 1	$\text{mm a}^{-1}$
Western fault initiation	10 – 18	2	Ma
Western fault initial slip rate	0.5 – 2.0	0.5 – 1	$\text{mm a}^{-1}$
Fault acceleration (of both faults)	3 – 6	1	Ma
PCF postacceleration slip rate	0.5 – 3.0	0.5 – 1	$\text{mm a}^{-1}$
western fault postacceleration slip rate	0.5 – 3.0	0.5 – 1	$\text{mm a}^{-1}$

<sup>a</sup>See section 5.2 for discussion of parameters as well as references.

### 5.2.1. Model Setup

[47] Our model setup consists of two cross sections corresponding to our sampling transects and structural cross sections across the Surla Range. Each transect is ~100 km wide, centered on the rift, and 4–5 km from north-south, just enough to encompass the samples for that transect. The model extends to 80 km depth, the modern thickness of the crust [Nábelek et al., 2009]. More details are given in Table 2, with explanation below. Topography is modeled as steady state, so uplift at the surface is balanced by erosion [e.g., Campani et al., 2010], though the Surla Range is a regional topographic high, the samples were taken from elevations similar to the surrounding terrain beyond the adjacent rift basins. Each model simulation begins at 20 Ma, although the models are insensitive to the duration of simulation before deformation initiates (at variable times). Configuration of Pecube is done completely through two text configuration files, `fault_parameters.txt` and `topo_parameters.txt`, which are well documented and included in the supporting information.

[48] Fault dip and thermal parameters are fixed during the formal iteration (constrained grid search). Sensitivity testing of these parameters is performed on the best constrained model following the formal inversion. This testing illustrates the influence that particular parameters have on the results. In an ideal situation, a full exploration of these parameters would occur as part of the iteration process, but because of the combinatoric nature of the parameters, including two values for a single parameter such as the radiogenic heat production rate doubles the number of models to be tested. However, unlike the fault

slip rate parameters, we iterate over, for which we have no prior knowledge save maximum allowable net extension, the thermal parameters produce geotherms comparable to elsewhere in Tibet, and the fault geometry is constrained by structural and seismic observations (see below for discussion).

### 5.2.2. Thermal Setup

[49] Our modeling has assumed a Moho temperature of 1200, radiogenic heating of  $20^\circ\text{C Ma}^{-1}$ , and a thermal diffusivity of  $20 \text{ km}^2 \text{Ma}^{-1}$  [Whittington et al., 2009]. The Moho temperature is consistent with estimates of 1069–1248°C from studies of middle Miocene xenoliths from the uppermost mantle (50–65 km depth, likely very close to the Moho before late Miocene crustal thickening) from the Sailipu area ~50 km west of the Lunggar rift [Liu et al., 2011]. The heat production value converts to heat production of  $2.39 \mu\text{W m}^{-3}$  for a granite with a density of  $2700 \text{ kg m}^{-3}$  and heat capacity of  $224.607 \text{ J mol}^{-1} \text{K}^{-1}$  (calculated at standard temperature and pressure using the equations of Whittington et al. [2009]). This heat production is low for granite [e.g., Förster and Förster, 2000] and lower than mean estimates for the Appalachian orogen of  $\sim 3 \mu\text{W m}^{-3}$  [Jaupart et al., 2007], which may be representative of Phanerozoic collisional orogens.

[50] These parameters lead to preextensional geothermal gradients of  $>40^\circ\text{C km}^{-1}$  in the upper crust, though the geothermal gradient relaxes rapidly with depth, so that it is  $<30^\circ\text{C km}^{-1}$  by 15 km below sea level (Figure 10). This geotherm is quite hot, at the high end of continental geotherms including those from volcanic provinces [e.g., Ehlers, 2005] though it is consistent with values estimated elsewhere in Tibet (Figure 10). Early model testing (part of model refinement before the formal iterative modeling) indicated that temperatures in the upper and middle crust are required to be this high in order to produce thermochronometer ages that match the observed values when exhumed by modeled faults matching our structural data. Because of the consistency with other Tibetan geothermal estimates (Figure 10) [Kapp et al., 2005a; Mechler et al., 2004], and because we consider it unlikely that the crust is much hotter than this hot model geotherm, we fix the thermal parameters during the formal iterative modeling. See section 5.3.2.2 for a further discussion of the thermal parameters, including model results where they have been changed.

### 5.2.3. Fault Setup

[51] Our model setup consists of two cross sections corresponding to our sampling transects and structural cross sections across the Surla Range (Figure 11). The northern transect (corresponding to cross section A-A') is modeled with an antilistic detachment fault on the west side (the SLD) that has a dip of  $8^\circ$  above the range,  $22^\circ$  at the rangefront, and  $45^\circ$  below 4 km depth, and a planar, moderate-angle ( $50^\circ$  dip) fault on the east side (the PCF). The southern transect (corresponding to cross section B-B') contains two planar moderate-angle faults, each with a dip of  $50^\circ$ .

[52] The velocity field in each model is calculated by Pecube internally from the geometry and slip rate prescribed for each fault in the Pecube configuration file (`fault_parameters.txt`); i.e., no velocity boundary conditions are applied to the model. An example velocity field for each model run due to different fault slip rates. Slip along a fault

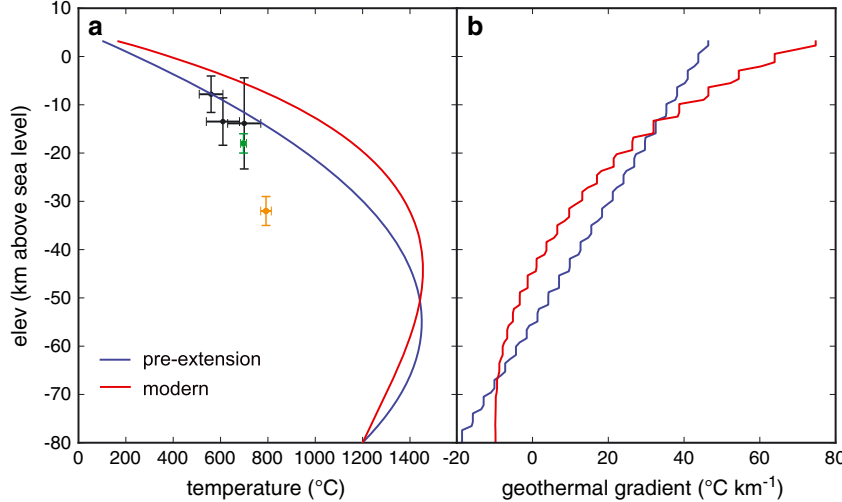


**Figure 10.** (a) Preextension and modern geotherm of the footwall of the SLD. Data points are other thermobarometric estimates. Black data are from petrologic studies in the Nyainqntanglha footwall [Kapp *et al.*, 2005a]. Green data point is from the  $\alpha$ - $\beta$  quartz transition in the Qiangtang block, and orange is the  $\alpha$ - $\beta$  quartz transition in the Lhasa block from seismic reflections [Mechie *et al.*, 2004]. (b) Preextension and modern geothermal gradient from the same location as Figure 10a. Steps in geothermal gradient are an artefact of the model and indicate the depth resolution of the model.

results in horizontal motions of the hanging walls and horizontal and vertical motions of the footwalls; no hanging-wall subsidence is included in our model, as hanging-wall subsidence would have a only a minor effect on our thermochronometer ages or the overall extension rates (which we are most interested in). We allow Pecube to update a fault's geometry due to slip on other faults in the model.

#### 5.2.4. Formal Iteration

[53] As we seek to constrain the slip histories of all major faults in the study area, we chose to explore a broad range of fault parameters (given in Table 2) that is enough to fully encapsulate the realistic geological possibilities. We allow for a Pliocene change in slip rate (positive or negative), as an acceleration has been suggested for other Tibetan rifts

[Dewane *et al.*, 2006; Hager *et al.*, 2006; Lee *et al.*, 2011; K. Sundell *et al.*, Evidence for constriction and Pliocene acceleration of east-west extension in the North Lunggar rift region of west-central Tibet, submitted to *Tectonics*, 2013]. Because the relationship between a thermochronometer age and the input parameters is nonlinear, it is necessary to iteratively model a large number of parameter combinations spanning the parameter space in order to rigorously estimate the probability distribution of the parameters. Our choice of fault parameters yields hundreds of thousands of combinations (each combination represents a unique faulting history), not including any variation in thermal parameters. Though the Pecube code is capable of running in an iterative “inversion” mode designed to seek the combination of parameters that

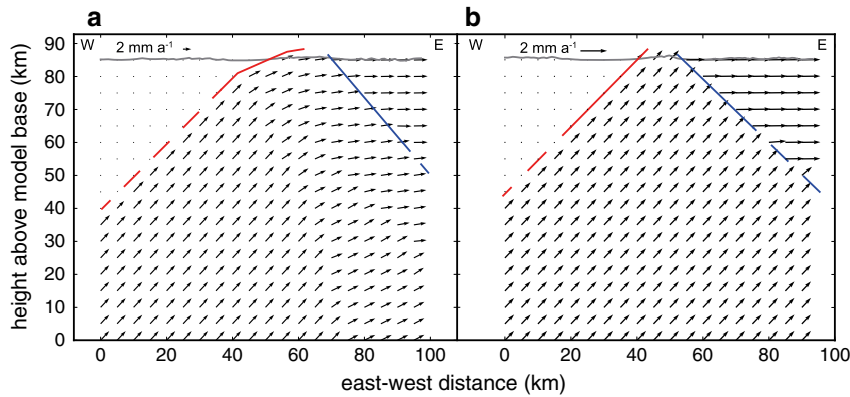


**Figure 11.** Cross sections through Pecube thermokinematic models showing the present-day geometries of the faults and example velocity fields relative to the western hanging walls. The velocity of the eastern hanging-wall basin reflects the overall extension rate for a given model run. Note that the orientation of the velocity fields in these models is a function of the slip rate on the faults and is therefore varied in each model simulation. Also note the change in velocity scale between the models. (a) Velocity field for example North Transect model run. (b) Velocity field for example South Transect model run.

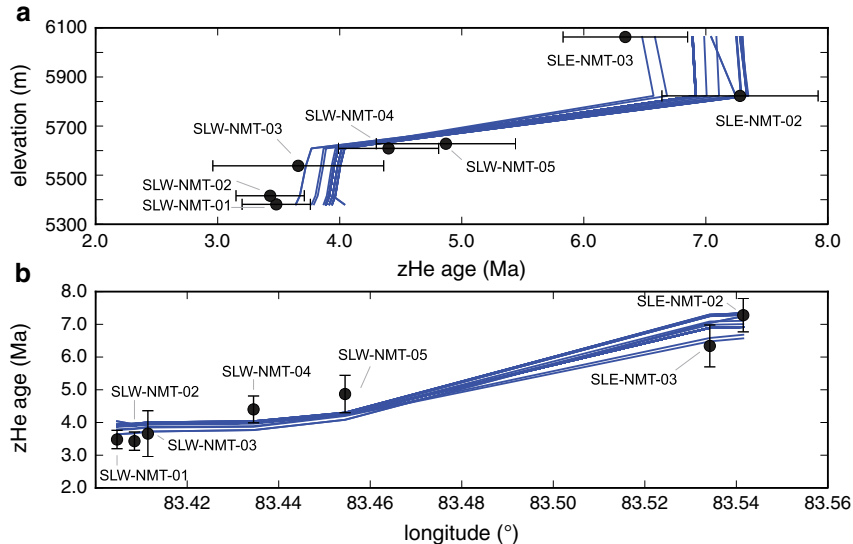


**Figure 12.** Pecube modeling results for north transect. (a) Age versus elevation plot for observed data (black dots with  $1\sigma$  error bars) and model results. Blue lines indicate predicted ages at each sample location for runs where all ages fit the data within  $2\sigma$ . (b) Age versus longitude plot for same data and predicted ages. Symbology same as Figure 12a.

best fits the observed (U-Th)/He cooling ages, our tests with it for the North Transect resulted in convergence towards combinations of parameters that were individually reasonable but yielded magnitudes of net extension that were unacceptably larger than our maximum estimates from geologic mapping; the code moved rapidly toward parameters resulting in 60 km net extension and varied little for hundreds of subsequent iterations (for interested readers, we have posted the results as “negative results”: [https://www.researchgate.net/publication/235332918\\_South\\_Lunggar\\_Rift\\_North\\_Transect\\_Pecube\\_NA\\_inversion\\_results](https://www.researchgate.net/publication/235332918_South_Lunggar_Rift_North_Transect_Pecube_NA_inversion_results)). Furthermore, with iterative nonlinear inversion techniques and a large parameter space, it can be difficult to ascertain that the parameter space was fully explored.

[54] Therefore, we chose to take all possible fault parameter combinations, calculate net extension for each combination, and only model those that yield magnitudes of extension consistent with our geologic cross sections. This yielded 10,397 model runs for the north transect and 13,998 model runs for the south transect out of hundreds of thousands of combinations before filtering. This is a large number of possible fault parameter combinations, but is the minimum number necessary to rigorously characterize the history of normal faulting in the SLR at a level of precision appropriate for the data. Fortunately, each model is independent of the others, so the problem lends itself well to running models in parallel on many processors; indeed, the number of independent computations qualifies this as an “embarrassingly parallel” computational problem in computer science parlance.

[55] In order to run the models in a time-efficient manner, we used PiCloud ([www.picloud.com](http://www.picloud.com)), a Python-based interface to Amazon's EC2 cloud servers. Identical Linux (Ubuntu 11.04) virtual environments were created on Amazon's servers, and Pecube v.3 was installed on each. A Python script was executed on a local machine that assembled and filtered the fault parameter combinations, edited the `fault_parameters.txt` file in the virtual environment, ran Pecube in the cloud via PiCloud for each

combination, and concatenated the resulting modeled thermochronometer ages for each sample. For further information on procedure or implementation, see the Python scripts in the supporting information, which are thoroughly commented. Although official statistics were not provided by PiCloud, the total run time versus individual run time suggests parallelization of 30–50× was achieved.

[56] We chose to filter our model results by testing each run to see if all output zHe model ages at the sample locations matched the observed cooling ages at either 1 or 2 standard deviations. Because many ages have very low standard deviations (possibly a consequence of a low aliquot sample size that does not represent the true uncertainty of the cooling age), we obtained no fits at  $1\sigma$  or  $2\sigma$  for either model. We refiltered the data, using the larger of the observed  $1\sigma$  value or an 8% uncertainty that represents the  $2\sigma$  standard error for the analytical standard (Fish Canyon Tuff) as the sample error in the modeling. All Pecube input files (configuration files, thermochronometer data, and elevation data), Python code, and binary (.npy) modeling results files are in the supporting information.

### 5.2.5. North Transect (A-A')

[57] The northern transect (Figure 11a) generally corresponds to cross section A-A' (Figure 8a; see Figure 17 for model location). 58 model runs fit the data at  $2\sigma$ , and none fit the data at  $1\sigma$  (Figure 12). Initiation of faulting occurred on the PCF first in all model runs and is distributed fairly equally between 10 and 16 Ma, with a median at 12 Ma and a mode at 10 Ma (Figures 16 and 17b). Initiation of the SLD is younger, with the majority of runs (48 out of 58, or 82%) showing an initiation at 8 Ma, with the remainder at 9 Ma.

[58] Initial extension rates (during initial PCF activity but before SLD initiation) were very low; all runs show the PCF slipping at  $0.25 \text{ mm a}^{-1}$ . Rapid extension began with the initiation of SLD slip, which has accommodated the large majority of extension across the SLR at this latitude. Results indicate initial slip on the SLD between  $1.5$  and  $3 \text{ mm a}^{-1}$ , with a median and strong mode at  $2.5 \text{ mm a}^{-1}$ . Because of the shallow

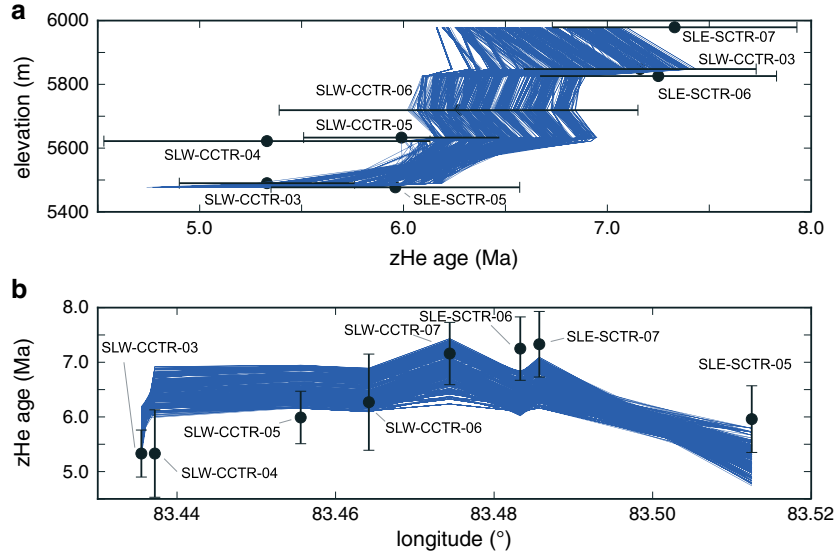


**Figure 13.** zHe data and Pecube model results for south transect. (a) Age versus elevation plot for observed data (black dots with  $1\sigma$  error bars) and model results. Blue lines indicate predicted ages at each sample location for runs where all ages fit the data within  $2\sigma$ . (b) Age versus longitude plot for same data and predicted ages. Symbology same as Figure 13a.

dip of this fault and the small contribution of the PCF to the horizontal extension rate, this is essentially the extension rate across the rift at this latitude (Figure 17a). Results do not strongly suggest a change in slip rate in the Pliocene; median and modal values stay the same, although the runs with low initial rates increased to the modal values (Figure 17a).

[59] Net extension is well constrained at 19–21 km, with only a few results between 19 and 20 km (Figure 17c). The median value is 20.62 km. Exhumation is also significantly greater in the west (due to the SLD) than in the east (due to the PCF). Exhumation of a sample currently at the SLD fault trace is ~10 km given our model geometry and 20 km of slip on the SLD (Figure 15). However, exhumation along the PCF is less, between 2 and 4 km for  $2\sigma$  fits. A vertical difference of 8 km exhumation over the 20 km width of the range yields a differential tilt of  $\sim 21^\circ$  to the east, indicating significant back rotation of the SLD footwall, consistent with many models of LANF and core complex evolution [e.g., Buck, 1991].

### 5.2.6. South Transect (B-B')

[60] The south transect model corresponds to cross section B-B' (Figure 8b; see Figure 15 for model location). The south transect had 786 model fits at  $2\sigma$  and none at  $1\sigma$  (Figure 13). Ages of fault initiation of both the PCF and the western fault are fairly similarly distributed between 10 and 18 Ma, with an increasing probability towards the younger ages (Figure 17e). Median initiations for both faults are 12 Ma. Modes for fault initiation are 11 Ma for the western fault and 10 Ma for the PCF (consistent with the northern model).

[61] Extension rates across the SLR for this model are more poorly constrained, between 0.5 and 3  $\text{mm a}^{-1}$ ; however, there are significantly more fits between 1 and 1.5  $\text{mm a}^{-1}$  (Figure 17d). Modal extension rates are 1.0  $\text{mm a}^{-1}$  for both before and after a possible Pliocene change in fault slip rate, also giving little support to post-Miocene acceleration. However, the later distribution is more skewed to the high end, and the median values change from 1.0 to 1.3  $\text{mm yr}^{-1}$ , owing to an increase in median slip rates (total slip, not simply horizontal

extension) of 0.5 to 1  $\text{mm a}^{-1}$  on the PCF; this acceleration has uniform distribution over the parameter space between 3 and 6 Ma. Median slip rates on the western fault are 1.0  $\text{mm a}^{-1}$  before and after an acceleration. Therefore, a subtle change in rate is not ruled out by the modeling, but is unlikely to be of significance.

[62] Net extension across this part of the SLR ranges from 10 to 16 km, with a higher probability at the high end (Figure 17f). As the two faults show similar initiation ages and slip rates, footwall tilt is unlikely to be significant, but slight rotation toward the east is possible, as the PCF may have initiated slightly later and slipped slightly more slowly in its early history (Figure 15).

### 5.2.7. Sensitivity Analysis of Fixed Model Parameters

[63] Though the possible fault slip rates and ages of fault initiation and acceleration were robustly tested in the previous section, the fault geometry and thermal parameters (radiogenic heat production and Moho temperature) were held fixed at values that produced good results in trials before the main testing phase and are in accordance with structural data from our mapping and geotherms from elsewhere in Tibet. Here we analyze these parameters to see how their variations affect our results. For these analyses, we use the northern transect with a faulting history that corresponds to the best model fit from the previous testing and individually vary one parameter at a time. The results (model ages) are compared to the best fit model and to the observed zHe ages.

#### 5.2.7.1. Variations in Detachment Geometry

[64] Although the geometry of the mylonitic shear zone is constrained by field observations in the exhumed footwall of the model, the geometry of the detachment at depth is not. As discussed in section 1.1, several models of detachment fault geometry exist. Here we run the prominent models (anticlinal, planar, and rolling hinge) as well as a model where the northern Surla Range is bound on the west by a planar high-angle normal fault (instead of the low-angle SLD), essentially testing our interpretation of the northern

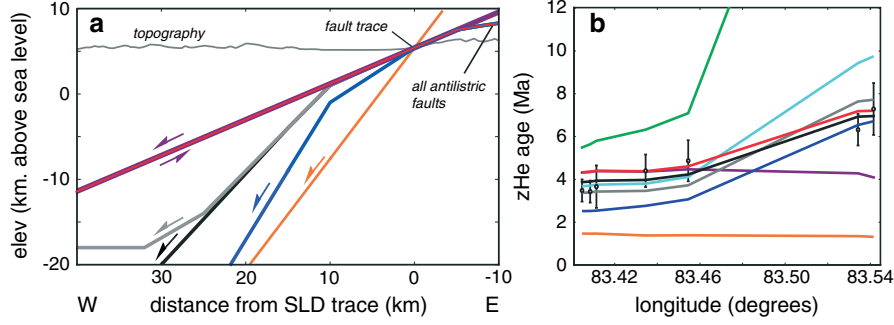


**Figure 14.** (a) SLD geometries tested during sensitivity testing. Orange = planar high angle. Blue = steep antilistic. Gray = rolling hinge. Black = moderate antilistic (used in main models). Red = low-angle antilistic. Purple = planar low angle. Red and purple faults have same subsurface geometry. All modeled faults daylight at mapped fault trace. No vertical exaggeration. (b) Results from sensitivity testing, presented as zHe age-longitude plot, with data as discrete points with 2-sigma error bars, and model results as lines connecting modeled ages at data point locations. Green = 1/2 modeled crustal heat production. Light blue = lower (900°C) Moho temperature. Other colors same as in Figure 14a.

Surla Range as a metamorphic core complex. As a point of clarification, references here to “antilistic” geometry refer to the decrease in dip of the detachment fault above the exhumed footwall of the range (leading to folding and flattening of the footwall), as opposed to the fault’s projection upward with the rangefront dip, which we call “planar.” We run two “antilistic” models: one with a low-angle geometry at depth (“low-angle antilistic”) and one with a high-angle geometry at depth (“high-angle antilistic”); the fault geometry in the previous section has this same antilistic upper detachment and subsurface dip in between these (“moderate-angle antilistic”). Then, we test the “rolling-hinge” model, with a shallow antilistic geometry and a listric geometry at depth. We also test two “planar” models, a “low-angle planar” and a “high-angle planar” model. Fault geometries are shown in Figure 14a.

[65] The results are shown in Figure 14b. All the antilistic models, including the rolling hinge, produce similar age versus longitude patterns, although only the moderate-angle antilistic model (used in the main model phase) fits all the data at  $2\sigma$ . The low-angle antilistic model produces ages that are  $\sim 1$  m.y. older than the observed ages near the western rangefront, but good fits to the east. The high-angle antilistic model produces ages that are  $\sim 1$  m.y. too young in the west and good fits in the east. The rolling-hinge model, with a moderate-angle ramp, produces ages that are in between these two models, similar to the moderate-angle antilistic model. These models all incorporate the same antilistic geometry, which produces older cooling ages into the footwall, as is observed in the data. In contrast, the planar fault models produce ages that are slightly younger into the footwall. The low-angle planar model produces ages that are  $\sim 1$  m.y. older than observations in the west (and identical to the low-angle antilistic model) but become 2–3 m.y. too young in the east. The high-angle model produces ages that are all younger than 2 Ma.

[66] The increase in model ages into the footwall in all antilistic models and the decrease in ages into the footwall in all planar models is consistent with previous studies [e.g., Kapp *et al.*, 2005a; Campani *et al.*, 2010; Robinson *et al.*, 2010]. It is easily explained by the recognition that, in antilistic models, preextensional sample locations have significant vertical separation, and therefore pass through the

PRZ at different times, and are rotated to roughly horizontal above the PRZ. In planar models, the footwall is not internally deformed, and the vertical separation of the samples remains constant; however, isotherms are convex upward in the footwall, as the footwall margins are cooled by the colder hanging wall. In all runs, steeper faults produce younger ages. We interpret this to indicate that a steeper fault exhumes deeper, and therefore hotter rocks; in other words, a steeper fault advects heat upward more efficiently.

[67] The results of this analysis show that the shallow geometry of the detachment fault has a great effect on the cooling ages, and that an antilistic geometry is necessary to reproduce the cooling patterns observed in the northern Surla Range; a planar geometry produces the opposite age-longitude trend. A similar cooling age pattern may be obtained by significant domino-style block rotation, as has been observed in Nevada [e.g., Stockli *et al.*, 2002]; however, this is not a possibility in the Surla Range given the opposing dip directions of the range-bounding normal faults. The model results also indicate that the dip of an antilistic detachment at depth does not have a large control on the thermochronometer ages [e.g., Ketcham, 1996], and therefore precise determination of this dip would require other methods. Although only the moderate-angle antilistic model fits the observations at  $1\sigma$ , it is quite likely that slight variations in the slip rate and timing parameters with other antilistic models could yield similarly good fits.

### 5.2.7.2. Variations in Thermal Parameters

[68] Varying the heat production to half its value,  $10^{\circ}\text{C Ma}^{-1}$ , caused a dramatic change in the modeled ages (Figure 14b). Given the colder resultant geotherm, faulting was insufficient to entirely exhume the footwall from below the preextensional zircon He partial retention zone. The samples near the trace of the SLD were exhumed from that depth, but are still several m.y. too old. Lowering the Moho temperature to  $900^{\circ}\text{C}$  leads to ages several m.y. too old in the eastern part of the footwall, but samples near the SLD trace were of acceptable age.

[69] The geothermal gradient in our preferred model is over  $40^{\circ}\text{ km}^{-1}$  in the upper several km of the crust before extension (Figure 10b). Within the footwall block near the detachment fault trace, rapid uplift and tectonic exhumation lead to vertical advection of heat and a compression of isotherms, giving a

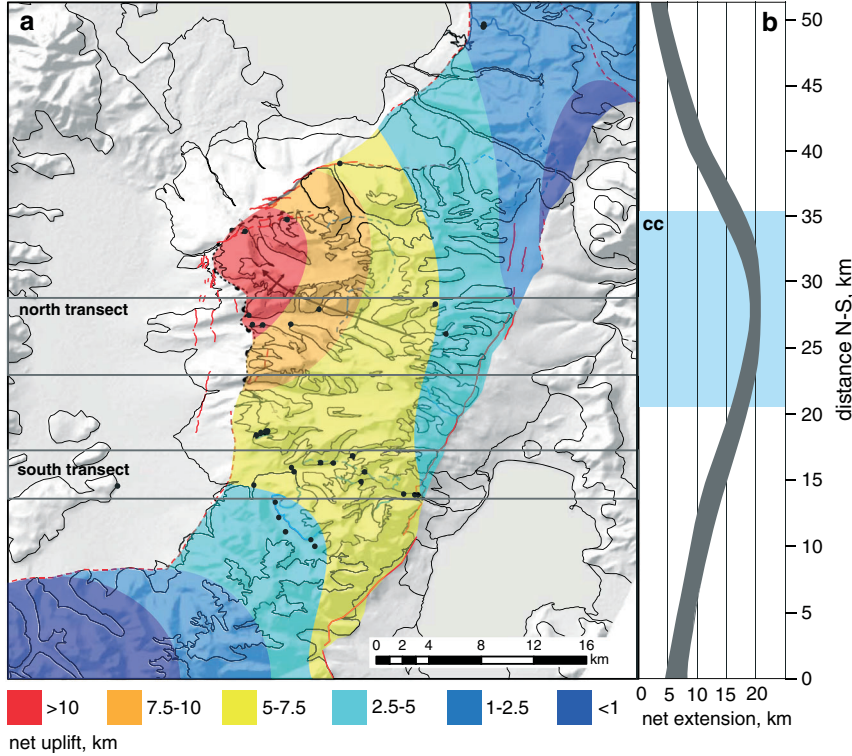


**Figure 15.** (a) Approximate contours of net uplift estimated from modeling results, zHe ages, and structural mapping. Also shown are zHe sample locations (dark gray dots), geologic structures, and contacts (see Figure 3 for symbology), and topography. Gray boxes show the width and location of the north and south transect Pecube models. Uncertainty in contour mapping is estimated at 2–5 km in both value and contour position based on variance in model results. (b) Net extension versus north-south distance from southern edge of map in Figure 15a; same scale as map. Dark gray band represents the 95% confidence interval, corresponding to the model results in Figures 12 and 13. Blue-gray box labeled “cc” indicates along-strike extent of core complex, as judged by low-angle brittle and mylonitic fault fabrics and domal geometry.

geothermal gradient of  $>70^\circ \text{ km}^{-1}$  in the shallowest crust. Though these geothermal gradients decrease rapidly with depth, the geotherm for the crust remains elevated.

[70] Because net extension in this preferred model is at the upper limit of what is acceptable given the structural constraints, it is not possible to increase the slip rates on the faults in order to compensate for a colder upper crust. While Tibet is almost uniformly declared to have a hot crust [e.g., Beaumont *et al.*, 2001; Francheteau *et al.*, 1984; Hu *et al.*, 2000; Kapp *et al.*, 2005a], the extremely high modeled temperatures in the lower crust are almost certainly too high. This may be the weakest result of our study. We suggest that radiogenic heat production in the crust is nonuniform and is probably greatly concentrated in the upper 10–20 km of the crust, due to pervasive intrusions of leucogranites [e.g., Kapp *et al.*, 2005a; Kapp *et al.*, 2008, this study] that are highly enriched in radioactive elements. However, it is not possible to implement depth-dependent radiogenic heating in the available version of Pecube.

## 6. Discussion

### 6.1. Evolution of the SLR

[71] The geology, thermochronology, and geochronology of the SLR indicate a rift characterized by a central horst block bounded by east- and west-dipping normal faults. In the

northern SLR, extension and exhumation are dominantly accommodated on the west-dipping SLD. Farther south, the east-dipping Palung Co fault becomes the dominant structure. Horizontal extension across the SLR ranges from 19–21 km at the latitude of the SLD to 10–16 km at the latitude of the southern transect. Extension decreases abruptly to the north and likely to the south as well, although perhaps more gradually. Extension rates also increase from south to north, from  $\sim 1 \text{ mm a}^{-1}$  to  $\sim 2.5 \text{ mm a}^{-1}$  at the latitude of the SLD. Fault initiation is broadly contemporaneous, though there is some probability of an earlier initiation in the south. The onset of more rapid extension in the north is much better constrained, and is most likely at  $\sim 8 \text{ Ma}$ , with the initiation of the SLD (Figure 16). Extensional faulting appears to have initiated during or a few million years after episodic magmatism in the rift; it is possible that thermal weakening associated with magmatism allowed for the onset of extension.

### 6.2. Comparison with the Nearby Rifts

[72] Observations and modeling results from the SLR are generally similar to the NLR [Kapp *et al.*, 2008; Sundell *et al.*, submitted manuscript, 2013]. ZHe ages from the NLD footwall are the same age or up to 1–2 m.y. younger than samples from the same relative position in the SLD footwall, likely indicating more rapid extension, although the detachment could be steeper at depth in the north or the crust

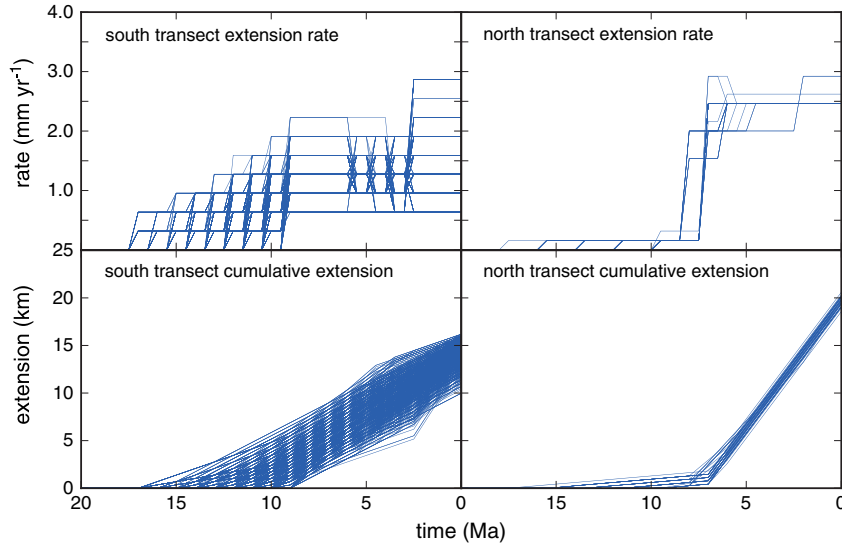


**Figure 16.** Extension rate and cumulative extension for north and south transect Pecube modeling results. Blue lines indicate model fits at  $2\sigma$ .

could be hotter. Furthermore, the structural and (U-Th)/He age distribution patterns in the NLR are much more continuous along strike (Sundell et al., submitted manuscript, 2013).

[73] The Lopukangri rift [Sanchez et al., 2013] shows a similar age of fault initiation of  $\sim 15$  Ma for the southernmost rift segment, which cuts the southern Gangdese range and structures of the Indus-Yarlung suture zone. The northern rift segment is undated, but the presence of supracrustal rocks (dominantly volcanic rocks) in the footwall suggests that exhumation is less than in the SLR. However, Quaternary normal fault scarps up to 350 m high suggest that modern rifting is rapid.

### 6.3. Thermal State of the Tibetan Crust

[74] The distribution of late Miocene to Pliocene zHe ages and the upper bounds on net extension across the SLR indicate moderate exhumation rates of very hot upper crust. The inference of hot crust is supported by a variety of observations. Volcanism and magmatism are ubiquitous in southern Tibet and appear to have continued at least until  $\sim 16$  Ma in the SLR. Younger ( $\sim 9$  Ma) leucogranites have been dated in the footwall of the NLR [Kapp et al., 2008]. Leucogranites give evidence of magmatism derived from low degrees of partial melting, as might be expected of a high overall geotherm, and the ultrapotassic volcanic rocks containing very hot upper mantle xenoliths [Liu et al., 2011] indicate that the basal temperatures were high as well. Hot springs in the NLR also provide independent evidence of elevated modern-day crustal heat flow, although these were not observed in the south. The “Zhongba” 2008 earthquakes on the Palung Co fault may give some idea of the local geotherm, as well. InSAR and teleseismic body wave modeling of the events give a centroid depth of  $\sim 8$ –9 km, with slip extending 3–4 km below that [Elliott et al., 2010; Ryder et al., 2012]. If the centroid depth lies just above the brittle-ductile transition, as is commonly inferred [e.g., Sibson, 1983; Ellis and Stöckhert, 2004], then temperatures may be  $\sim 350^\circ$  at that depth, which is well in agreement with our model away from the detachment footwall where the geotherm is elevated due to ongoing exhumation (Figure 10).

[75] Evidence for high crustal temperatures from outside the Lunggar region is widespread. We observed geysers near Raka, along the Indus-Yarlung Suture Zone, at approximately  $29.60^\circ\text{N}$ ,  $85.75^\circ\text{E}$ . Francheteau et al. [1984] estimated high heat flow from elevated temperatures in lake sediment boreholes in south-central Tibet, south of the Indus-Yarlung Suture Zone. Thermobarometry in the Nyainqntanglha rift [Kapp et al., 2005a] indicates temperatures within error of our preextensional geotherms (Figure 10). Meechie et al. [2004] located the  $\alpha$ - $\beta$  transition in quartz at  $\sim 17$  km in the Qiangtang block through seismic methods, indicating an elevated geotherm there (mean geothermal gradient  $39^\circ\text{C km}^{-1}$ ), although in the Lhasa block, they found more typical temperatures (mean geothermal gradient  $25^\circ\text{C km}^{-1}$ ). Hu et al. [2000] interpolated heat flow observations over the plateau and found very high values ( $> 350 \text{ mW m}^{-2}$ ) in the Yadong-Gulu rift and moderately high values to the west, although observations are sparse; a similar study by Wang [2001] showed the plateau to have a high mean heat flow of  $\sim 80 \text{ mW m}^{-2}$ . The same argument outlined above for elevated temperatures evidenced by shallow seismicity holds for the entire plateau [e.g., Molnar and Chen, 1983; Molnar and Lyon-Caen, 1989; Priestley et al., 2008; Wei et al., 2010] and is supported by the short wavelength of rift-flank uplifts indicating a long-term effective elastic thickness of only 2–4 km [Masek et al., 1994]. Elevated heat flow is a necessary condition for large-scale lower-crustal flow, which has been commonly inferred to explain flat topography and extension within the plateau itself [e.g., Cook and Royden, 2008], ductile injection into eastern Tibet [e.g., Clark and Royden, 2000], and extrusion through the Himalaya [e.g., Beaumont et al., 2001; Nelson, et al., 1996]. Evidence consistent with partial melt in the crust is given by seismic reflections [e.g., Nelson et al., 1996], low  $V_p/V_s$  ratios [e.g., Hirn et al., 1995] and widespread leucogranite magmatism [Kapp et al., 2005a, 2008; Sanchez et al., 2013; this study].

[76] A hot and mobile middle to lower crust may be a necessary condition for the formation of metamorphic core complexes [e.g., Buck, 1988] and is very likely to be

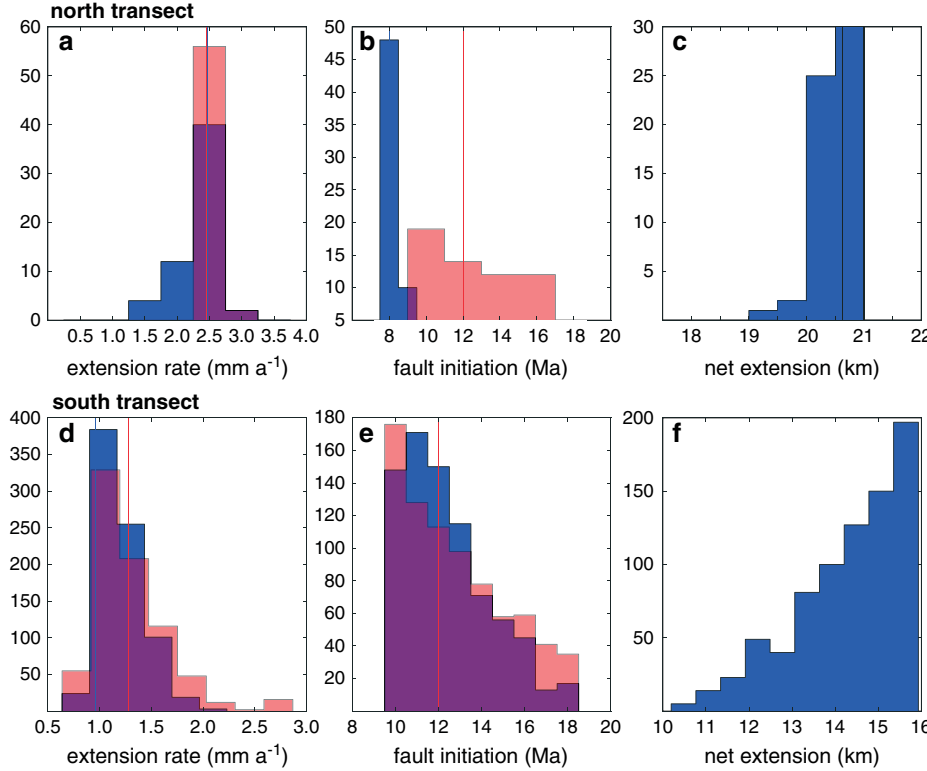


**Figure 17.** Histograms for model run results. (a) Horizontal extension rate for the northern transect (A-A') before (blue) and after (red) a possible Pliocene acceleration for the northern transect. Purple in all graphs indicates overlap of red and blue histograms, and vertical lines indicate median values. (b) Fault initiation ages for the SLD (blue) and PCF (red). (c) Net extension across the northern SLR. (d) Horizontal extension rate for the southern transect (B-B') before (blue) and after (red) a possible Pliocene acceleration. (e) Initiation ages for the western fault (blue) and PCF (red). (f) Net extension across the southern SLR.

responsible for the lack of a major regional lowering of topography around the Lunggar rift, despite large amounts of crustal thinning and extension [Block and Royden, 1990]. The mobile crust would be able to flow laterally into the extending region to mitigate the gravitational potential energy contrasts that would be produced by the steep topographic gradients from the crustal thinning. That said, the relatively high number of large lakes, both near the rift and within rift basins bound by moderate to high-angle normal faults (but not the supradetachment basins [Kapp et al., 2008]), may be indicative of minor regional subsidence, as nearby crust is drawn into the actively uplifting core complex footwalls. This phenomenon, on a larger scale, has been suggested to explain subsidence of the Zhada basin in the Indian Himalaya between the Leo Pargil and Gurla Mandhata core complexes [Saylor et al., 2010].

#### 6.4. Implications for Rift and Detachment Fault Development

[77] The SLD is unlike many detachment faults in that core-complex type deformation is a relatively localized phenomenon; the western range-bounding normal fault in the central and southern Lunggar rift is  $\sim 70\text{--}80$  km north-south (not taking into account curves in the fault trace), though the SLD and core complex are only about 15 km N-S. However, despite the relatively restricted areal extent of

the SLD, it has accommodated greater and more rapid extension and exhumation than any other fault in the SLR. Additionally, faulting along the western rangefront transitions from a typical moderate to high-angle normal fault geometry in the south, to low angle, and then back to high angle in the north. Most of the mapped detachment faults in the western US and elsewhere remain at low angle along strike and are either buried or truncated by other faults on their ends, so the transition from low to high angle is not observed. Some analogs exist: the NLR [Kapp et al., 2008], the Dixie Valley fault (Nevada) [Caskey et al., 1996], the Cañada David detachment, Baja, Mexico [Axen et al., 2000; Fletcher and Spelz, 2009], possibly the Mount Suckling-Dayman Dome metamorphic core complex [Daczko et al., 2011], and segments of the Kenya rift [Morley, 1999] show an along-strike transition from high to low-angle normal faulting, with along-strike widths of low-angle faulting similar to the SLD. All of these, including the SLD, are associated with magmatism during or immediately preceding extension. However, magmatism may not be exclusive to the region of detachment faulting; certainly in the SLR, two dated samples are insufficient to fully constrain the extent of Miocene magmatism. These observations show that LANF and core complex development is not a distinct mode of rifting, nor that it will be the dominant extensional mode in a certain geodynamic environment (such as rapid extension in hot, thick crust). Instead, it is an end-member

in the spectrum of rifting, but one that is generally associated with high magnitudes of extension and exhumation [e.g., Abers, 2001; Forsyth, 1992], as well as synkinematic magmatism [Parsons and Thompson, 1993].

[78] The large along-strike variation in uplift and extension over fairly short distances in the SLR (Figure 15) is striking, but is well constrained by the structural and thermochronological observations and modeling. This extension gradient must be accommodated by deformation of the hanging wall, though no suitable structures were observed. A zone of distributed dextral shear to the northwest of the SLD may be present, but difficult to observe due to the cover of water, thick moraine and alluvium.

### 6.5. Timing and Rates of Tibetan Extension

[79] Our results in the SLR suggest a minimum age for the onset of extension in southwestern Tibet of  $\sim$ 16–12 Ma (Figures 16 and 17). Furthermore, we find evidence of a rapid increase in extension rate at  $\sim$ 8 Ma in the northern part of the rift, as slip on the SLD began. These results are consistent with, and may reconcile, the few other studies of rifting within the Tibetan plateau. The modeled age of rift initiation here is similar to the results of Blisniuk *et al.* [2001] which uses cross-cutting relationships to provide a minimum age of the onset of rifting in central Tibet. Our results give a similar regional minimum, in that activity may have begun earlier on a nearby rift. However, our combination of thermal and structural constraints (limiting maximum extension) provides both upper and lower bounds on initiation of the SLR itself. Our suggestions of rapid extension related to slip on the SLD are also consistent with work on the Nyainqntanglha segment of the Yadong-Gulu rift indicating a phase of rifting beginning at 8 Ma [Harrison *et al.*, 1995; Kapp *et al.*, 2005a]. The thermal histories of samples in the footwall of the Nyainqntanglha detachment show a rapid latest Miocene to early Pliocene cooling event related to exhumation of the range due to slip on a high-angle normal fault [Harrison *et al.*, 1995] or on the detachment itself [Kapp *et al.*, 2005a]; the more recent interpretation is supported by seismic imaging of the rift showing the detachment to continue uncut and at a low angle below the supradetachment basin, and to project to active fault scarps at the rangefront [Cogan *et al.*, 1998]. However, evidence of higher-temperature cooling ( $>300^{\circ}\text{C}$ ) in the middle Miocene is seen in their thermochronology data as well, and the footwall rocks would have had to have cooled through  $350^{\circ}\text{C}$  in the middle Miocene if the mylonitic shear zone was formed during the current extensional phase. A scenario involving slow deformation beginning in the mid-Miocene followed by acceleration, involving slip on large-magnitude detachment faults, at  $\sim$ 8 Ma is consistent with all data sets. While there is no compelling reason to assume a priori that extension in the SLR and Nyainqntanglha should be contemporaneous, the larger data set and more thorough thermal modeling from the SLR show how an earlier and slower phase of extension preceding an acceleration could be masked due to sparse sampling and the restricted thermal modeling limited by older computing technology.

[80] The structural and thermochronological data from the footwalls of the SLD, NLD [Kapp *et al.*, 2008], and Nyainqntanglha detachment [Harrison *et al.*, 1995; Kapp

*et al.*, 2005a] involve an earlier phase of ductile deformation with superposed brittle deformation. Ratschbacher *et al.* [2011] combine evidence of Miocene ductile deformation and Pliocene-present brittle deformation from throughout the orogen and suggest that two distinct deformational events occurred in Tibet, and that the earlier, ductile event is not necessarily related to crustal extension. However, given that the normal-sense ductile shear occurs in detachment footwalls of rifts showing evidence of active extensional deformation (e.g., seismicity, Quaternary fault scarps with at least 10s of meters of throw), we prefer the interpretation that the change from ductile to brittle deformation is a consequence of progressive exhumation and cooling of the footwall. Similar interpretations have been made for the NLD [Kapp *et al.*, 2008], the Nyainqntanglha detachment [Kapp *et al.*, 2005a], Ama Drime detachment [Langille *et al.*, 2010] and for many detachment faults in the Basin and Range [e.g., Wernicke, 1981; Davis, 1983], the Aegean [e.g., Lee and Lister, 1992], the Alps [e.g., Campani *et al.*, 2010], and Peru [e.g., McNulty and Farber, 2002].

### 6.6. Contribution to the Tibetan Strain Budget

[81] As discussed in section 1.2.2, some estimates have been made for net extension in Tibet. Given  $\sim$ 20 km extension for the SLR and about 10 km for the Pum Qu-Xainza and Tangra Yum Co rifts, and assuming small ( $\sim$ 1 km) contribution from the various smaller rifts in the Lhasa block at the latitude of the SLR, we may broadly estimate net extension at 50–70 km. However, our results from the SLR show that along-strike variation can be significant, and therefore that applying a single or narrow range of values for Tibetan extension may be problematic.

[82] Extension rates across the plateau are better constrained over the decadal scale by GPS geodesy. Zhang *et al.* [2004] measured  $21.6 \pm 2.5 \text{ mm a}^{-1}$  extension between  $79^{\circ}$  and  $95^{\circ}$  E longitude, or roughly the area showing N-trending rifts. The sites SHIQ and TCOQ are located  $\sim$ 400 and  $\sim$ 150 km to the west and east of the SLR, respectively, and have a  $100^{\circ}$  component of  $1.0 \pm 1.3$  and  $4.6 \pm 3.5 \text{ mm a}^{-1}$ , yielding  $3.6 \pm 4.8 \text{ mm a}^{-1}$  extension across the western Lhasa block [Zhang *et al.*, 2004]. Though this figure is very imprecise, it gives a most probable value that is about  $1 \text{ mm a}^{-1}$  higher than extension across the SLR, suggesting that the Lunggar rift is the dominant extensional structure in the western Lhasa block. Interestingly, it also suggests that extension rates are considerably higher in the eastern Lhasa block; this is supported by the analysis of Gan *et al.* [2007] using GPS data from throughout the orogen. These comparisons assume that deformation rates may be compared from the 10 year scale to the  $10^6$  year scale; our modeling is not sufficient (or intended) to resolve high-frequency changes in slip rate due to the earthquake cycle, fault interaction, or other processes.

[83] Support for both block-type [e.g., Meade, 2007; Thatcher, 2007] and continuum deformation [e.g., England and Houseman, 1988; Cook and Royden, 2008] can be found in the results from the SLR. Block-type deformation is supported by the results that the SLR has accommodated  $\sim$ 10–20 km of localized extension, which is of regional significance, and likely the majority of the extension that has occurred at that latitude in the western Lhasa block; therefore, the SLR bounds regions that are deforming at a much lower rate. However, the rapid along-strike variation

in rates and magnitudes of extension are possibly accounted for by extension on neighboring normal faults (known or not), or diffuse deformation within the adjacent crust; in this case, extensional strain would be penetrative at a regional scale. Therefore, extensional strain is present throughout the western Lhasa block, but concentrated at the Lunggar rift; essentially, strain is localized at rift zones instead of individual faults. This is in contrast to the preferred model of Loveless and Meade [2011], who consider the western Lhasa block to be essentially undeforming. However, given the lack of published slip rates across the Lunggar rift at the time that study was performed, the omission is understandable. The specific results here are consistent with the more general conclusion of Loveless and Meade [2011] that deformation type is spatially variable, with different areas occupying different positions on the continuum-rigid block spectrum. The observed distributed extension from the SLD through the Lopukangri rift and to the smaller graben to the east [Murphy et al., 2010] is consistent with studies predicting or observing wide zones of extension in areas of hot and weak crust [Buck, 1988; Kogan et al., 2012].

## 6.7. Causes for Tibetan Extension

[84] Extension in Tibet has been attributed to a variety of causes. Thorough reviews of many of these have been published recently [Lee et al., 2011; Ratschbacher et al., 2011], and we will not attempt to replicate these efforts, as our results are from a small area and are in broad agreement with published work. However, we will discuss the implications of our results with respect to several prominent models that involve timing constraints.

[85] Convective removal of mantle lithosphere is commonly inferred to explain the elevation and extension of the plateau [e.g., Molnar et al., 1993; England and Houseman, 1988]. This hypothesis is generally supported by geophysical studies indicating a hot upper mantle under the Qiantang block with low Vp/Vs and Poisson's ratios [e.g., Owens and Zandt, 1997]; colder mantle lithosphere under southern and far northern Tibet is quite reasonably explained as postremoval underthrusting of Indian and Tarim lithosphere. The timing of convective removal was earlier considered to occur at ~8 Ma, largely due to the work of Molnar et al. [1993], Pan and Kidd [1992], and Harrison et al. [1995]; more recently, this date has been allowed to be pushed back by several million years to explain the Miocene deceleration of Indo-Asian convergence rate [Molnar and Stock, 2009]. Recent studies of mantle xenoliths in south Tibetan ultrapotassic rocks [e.g., Liu et al., 2011] show that the upper mantle was very hot and metasomatized by ~17 Ma, strongly suggesting that removal of mantle lithosphere was underway by this time. Therefore, an increase in elevation (and excess gravitational potential energy) shortly after this time may explain the middle Miocene onset of extension in central and western Tibet [Blisniuk et al., 2001; this study] and in the Nyainqntanglha rift [Harrison et al., 1995] should an early phase of extension have occurred. However, if convective removal occurred in the early-middle Miocene and explains extension and Indo-Asian convergence rate reduction [Molnar and Stock, 2009], then it cannot explain rapid extension beginning at 8 Ma [Harrison et al., 1995; Kapp et al., 2005a; this study].

[86] Yin [2000] suggested that the synchronous onset of extension from southern Tibet and the Himalaya north through Lake Baikal resulted from a subcontinental scale change in boundary conditions, which he attributed to rollback of the Pacific slab subducting below Eurasia. This timing was later revised to ~15 Ma, in accordance with the observed cessation of backarc seafloor spreading in the East China Sea [Yin, 2010]. This hypothesis is consistent with the onset of Tibetan extension, although the ability of the crust to transmit extensional stresses over >1000 km (from the Pacific coast across China to Tibet) is questionable, given the low theoretical tensile strength of the crust [England et al., 1985]; stress transmission may be aided by east-directed compression on the South and East Chinese cratons due to the Tibetan plateau's excess gravitational potential energy [Kong and Bird, 1996]. Furthermore, the change from tension to compression across the western Pacific subduction zones in the late Miocene indicates that another mechanism, such as east-directed asthenospheric flow from beneath the Tibetan plateau is responsible [Yin, 2010; Yin and Taylor, 2011], although estimates for the initiation of this flow have not yet been made.

[87] In their work considering various changes to Tibetan geodynamics that may induce extension, England and Houseman [1988] discuss how a reduction in Indo-Asian convergence rate could lead to extension; essentially, N-S compressional stress is linearly related to convergence rate, and a reduction in the former would lead to a reduction in the latter. Though they discount this possibility on the grounds that their models show the decrease would have to be far more drastic than the contemporaneous data allowed for, we suggest otherwise. The presence of both normal and strike-slip faulting, both accommodating E-W extension, indicate that the N-S compressional stress and vertical compressional stress are close to equal, whereas the E-W stress is the minimum compressive stress [Molnar and Lyon-Caen, 1989]; the change between normal faulting and strike-slip faulting may be related to modest changes in vertical stress related to local variations in elevation [Elliott et al., 2010; Styron et al., 2011b]. This modern near-equilibrium between N-S and vertical stress suggests that a decrease in N-S stress in the middle Miocene due to convergence deceleration may be sufficient to initiate extension. Coeval with the mid-Miocene onset of extension on the high plateau is a change from N-S thrusting to strike-slip faulting along E-W striking faults in northern Tibet [Lease et al., 2011], also consistent with a decrease in N-S compression (or an increase in vertical stress). However, middle Miocene Indo-Asian convergence rate decrease does not explain the extensional acceleration at 8 Ma, either.

[88] It should be noted that none of these models are mutually exclusive, and some of them may be linked, such as the hypothesis that delamination and uplift caused the Indo-Asian convergence deceleration [Molnar and Stock, 2009]. Additionally, because the estimates of timing and rates of Tibetan extension are constrained by sparse data of different types, testing of these models for Tibetan extension may not be possible with sufficient resolution to falsify any of them. However, none of these models explain the observed rapid extension at 8 Ma. As this is based on only two data points, it is unclear whether this is a local signal relating to (for example) detachment fault evolution, or whether it represents a regionally extensive signal.

## 7. Conclusions

[89] We provide the first geologic mapping and zircon U-Pb geochronology and zircon (U-Th)/He thermochronology of the SLR in western Tibet. The SLR is a large N-S trending active rift and is the southern segment of the Lunggar rift, likely the major extensional structure in southwestern Tibet. Robust thermokinematic modeling with Pecube (~25,000 simulations) indicates that extension initiated in the middle Miocene (16–12 Ma) and accelerated in the late Miocene (~8 Ma). Significant along-strike variation exists in deformation rates; horizontal extension rates are ~1 mm a<sup>-1</sup> in the south and 2.5 mm a<sup>-1</sup> in the north, and net extension is between ~10 and 21 km, respectively. The lower rates and magnitudes of extension in the southern SLR correlate with higher-angle normal faulting, while the higher rates and magnitudes correlate with the SLD, a fairly narrow (~15 km along-strike) low-angle normal fault that has exhumed a metamorphic core complex. Testing of multiple fault geometries indicates that an antilistic geometry of the upper SLD (shallowing to subhorizontal; i.e., the upper hinge of a rolling hinge) is necessary to reproduce the zHe cooling age distribution; although several subsurface geometries are permissible, the best fit was provided by a detachment geometry that steepens to moderate angles at depth. Our results also show that the Tibetan crust is very hot; preextensional geothermal gradients are ~40°C km<sup>-1</sup> in the upper several km of the crust, and currently higher within the footwall of the SLD. Though several geodynamic models may explain the timing of rift initiation in the SLR in the early to middle Miocene, none so far explain the onset of rapid extension at 8 Ma.

[90] **Acknowledgments.** RS thanks Jhoma Tsering and her associates for help in the field, and Roman Kislytsyn and the KU IGL group for laboratory assistance. Jean Braun, Frederic Herman, and Dave Whipp provided useful advice about Pecube modeling. Discussions with Tandis Bidgoli, Paul Kapp, and Chris Morley proved enlightening. We thank Doug Walker for his encouragement in pushing us to test between magma emplacement and faulting as the cause of mylonitization. This manuscript, especially of modeling description, benefited greatly from careful reviews and comments by Tectonics editor Todd Ehlers, associate editor Frederic Herman, reviewers Gweltaz Mahéo and Marion Campani, and an anonymous reviewer. This work was supported by Tectonics Division of the National Science Foundation (grants EAR-0809408 and EAR-0911652). The conclusions of this work do not necessarily represent those of the NSF.

## References

- Abers, G. A. (2001), Evidence for seismogenic normal faults at shallow dips in continental rifts, *Geol. Soc. Spec. Publ.*, 187(1), 305–318, doi:10.1144/GSL.SP.2001.187.01.15.
- Abers, G. A., A. Ferris, M. Craig, H. Davies, A. L. Lerner-Lam, J. C. Mutter, and B. Taylor (2002), Mantle compensation of active metamorphic core complexes at Woodlark rift in Papua New Guinea, *Nature*, 418(6900), 862–865, doi:10.1038/nature00990.
- Andersen, T. (2002), Correction of common lead in U–Pb analyses that do not report 204 Pb, *Chem. Geol.*, 192, 59–79.
- Anderson, E. M. (1951), *The Dynamics of Faulting. Etc. (Revised)*, Edinburgh, London.
- Armijo, R., P. Tappognier, J. L. Mercier, and H. Tong-Lin (1986), Quaternary extension in southern Tibet: Field observations and tectonic implications, *J. Geophys. Res.*, 91, 13,803–13,872.
- Armstrong, R., and P. Ward (1991), Geographic patterns of Cenozoic magmatism in the North American Cordillera: The temporal and spatial association of magmatism and metamorphic core complexes, *J. Geophys. Res.*, 96(B8), 13,201–13,224.
- Axen, G. J., and J. M. Bartley (1997), Field tests of rolling hinges: Existence, mechanical types, and implications for extensional tectonics, *J. Geophys. Res.*, 102(B9), 20,515–20,520.
- Axen, G. J., M. Grove, A. Rothstein, M. Fletcher, and L. Abbott (2000), Thermal evolution of Monte Blanco dome: Low-angle normal faulting during the Gulf of California rifting and late Eocene denudation of the eastern Pensinsular Ranges, *Tectonics*, 19(2), 197–212.
- Beaumont, C., R. Jamieson, M. H. Nguyen, and B. Lee (2001), Himalayan tectonics explained by extrusion of a low-viscosity crustal channel coupled to focused surface denudation., *Nature*, 414(6865), 738–742, doi:10.1038/414738a.
- Bendick, R., and L. Flesch (2007), Reconciling lithospheric deformation and lower crustal flow beneath central Tibet, *Geology*, 35(10), 895–898, doi:10.1130/G23714A.1.
- Blisniuk, P. M., B. R. Hacker, J. Glodny, L. Ratschbacher, S. Bi, Z. Wu, M. O. McWilliams, and A. Calvert (2001), Normal faulting in central Tibet since at least 13.5 Myr ago., *Nature*, 412(6847), 628–32, doi:10.1038/35088045.
- Block, L., and L. H. Royden (1990), Core complex geometries and regional scale flow in the lower crust, *Tectonics*, 9(4), 557–567.
- Bosworth, W. (1985), Geometry of propagating continental rifts, *Nature*, 316(6029), 625–627, doi:10.1038/316625a0.
- Braun, J. (2003), Pecube: A new finite-element code to solve the 3D heat transport equation including the effects of a time-varying, finite amplitude surface topography, *Comput. Geosci.*, 29(6), 787–794, doi:10.1016/S0098-3004(03)00052-9.
- Braun, J., et al. (2012), Quantifying rates of landscape evolution and tectonic processes by thermochronology and numerical modeling of crustal heat transport using PECUBE, *Tectonophysics*, 524–525, 1–28, doi:10.1016/j.tecto.2011.12.035.
- Brun, J., D. Sokoutis, and J. Van Den Driessche (1994), Analogue modeling of detachment fault systems and core complexes, *Geology*, 22(5), 319–322.
- Buck, W. R. (1988), Flexural rotation of normal faults, *Tectonics*, 7(5), 959–973.
- Buck, W. R. (1991), Modes of continental lithospheric extension, *J. Geophys. Res.*, 96(B12), 20,161–20,120.
- Burchfiel, B., and L. H. Royden (1985), North-south extension within the convergent Himalayan region, *Geology*, 13(10), 679–682.
- Burg, J. P., and G. M. Chen (1984), Tectonics and structural zonation of southern Tibet, China, *Nature*, 311, 219–223.
- Campani, M., F. Herman, and N. Mancktelow (2010), Two-and three-dimensional thermal modeling of a low-angle detachment: Exhumation history of the Simplon Fault Zone, central Alps, *J. Geophys. Res.*, 115, B10420, doi:10.1029/2009JB007036.
- Caskey, S., S. Wesnousky, P. Zhang, and D. Slemmons (1996), Surface faulting of the 1954 Fairview Peak (Ms 7.2) and Dixie Valley (Mw 6.8) earthquakes, central Nevada, *Bull. Seismol. Soc. Am.*, 86(3), 761–787.
- Clark, M. K., and L. H. Royden (2000), Topographic ooze: Building the eastern margin of Tibet by lower crustal flow, *Geology*, 28(8), 703–706, doi:10.1130/0091-7613(2000)28<703.
- Cogan, M. J., et al. (1998), Shallow structure of the Yadong-Gulu rift, southern Tibet, from refraction analysis of Project INDEPTH common midpoint data, *Tectonics*, 17(1), 46–61.
- Cook, K. L., and L. H. Royden (2008), The role of crustal strength variations in shaping orogenic plateaus, with application to Tibet, *J. Geophys. Res.*, 113, B08407, doi:10.1029/2007JB005457.
- Copley, A., and D. McKenzie (2007), Models of crustal flow in the India-Asia collision zone, *Geophys. J. Int.*, 169, 683–698.
- Copley, A., J.-P. Avouac, and B. P. Wernicke (2011), Evidence for mechanical coupling and strong Indian lower crust beneath southern Tibet, *Nature*, 472(7341), 79–81, doi:10.1038/nature09926.
- Crittenden, M. D., Jr., P. J. Coney, and G. H. Davis (Eds.) (1980), *Cordilleran Metamorphic Core Complexes*, Mem. Geol. Soc. Am. 153, 490 p.
- Daczko, N. R., P. Caffi, and P. Mann (2011), Structural evolution of the Dayman dome metamorphic core complex, eastern Papua New Guinea, *Geol. Soc. Am. Bull.*, 123(11–12), 2335–2351, doi:10.1130/B30326.1.
- Daoudene, Y., D. Gapais, G. Ruffet, E. Gloaguen, A. Cocherie, and P. Ledru (2012), Syn-thinning pluton emplacement during Mesozoic extension in eastern Mongolia, *Tectonics*, 31, TC3001, doi:10.1029/2011TC002926.
- Davis, G. H. (1983), Shear-zone model for the origin of metamorphic core complexes, *Geology*, 11(6), 342–347, doi:10.1130/0091-7613(1983)11<342.
- DeCelles, P. G., D. M. Robinson, and G. Zandt (2002), Implications of shortening in the Himalayan fold-thrust belt for uplift of the Tibetan Plateau, *Tectonics*, 21(6), 1062, doi:10.1029/2001TC001322.
- DeCelles, P. G., P. Kapp, J. Quade, and G. E. Gehrels (2011), Oligocene-Miocene Kailas basin, southwestern Tibet: Record of postcollisional upper-plate extension in the Indus-Yarlung suture zone, *Geol. Soc. Am. Bull.*, 123(7–8), 1337–1362, doi:10.1130/B30258.1.
- Dewane, T. J., D. F. Stockli, C. Hager, M. Taylor, L. Ding, J. Lee, and S. Wallis (2006), Timing of Cenozoic E-W extension in the Tangra Yum Co-Kung rift, south-central Tibet, *Eos. Trans. AGU*, 87(52), Fall Meet. Suppl., Abstract T34C-04.

- Dewey, J. F., R. M. Shackleton, C. Chengfa, and S. Yiyin (1988), The tectonic evolution of the Tibetan Plateau, *Philos. Trans. R. Soc. London, Ser. A*, 327(1594), 379–413.
- Ding, L., P. Kapp, D. Zhong, and W. Deng (2003), Cenozoic volcanism in Tibet: Evidence for a transition from oceanic to continental subduction, *J. Petrol.*, 44(10), 1833–1865, doi:10.1093/petrology/egg061.
- Ding, L., P. Kapp, and X. Wan (2005), Paleocene-Eocene record of ophiolite obduction and initial India-Asia collision, south central Tibet, *Tectonics*, 24, TC3001, doi:10.1029/2004TC001729.
- Dodson, M. (1973), Closure temperature in cooling geochronological and petrological systems, *Contrib. Mineral. Petrol.*, 17(8), 444, doi:10.2307/495689.
- Duebendorfer, E. M., J. E. Faulds, and J. E. Fryxell (2010), The South Virgin–White Hills detachment fault, southeastern Nevada and northwestern Arizona: Significance, displacement gradient, and corrugation formation, in *Miocene Tectonics of the Lake Mead Region, Central Basin and Range*, edited by P. J. Umhoefer et al., *Spec. Pap. Geol. Soc. Am.*, 463, pp. 275–287, doi:10.1130/2010.2463(12).
- Edwards, M., and L. Ratschbacher (2005), Seismic and aseismic weakening effects in transtension: Field and microstructural observations on the mechanics and architecture of a large fault zone in SE Tibet, *Geol. Soc. Spec. Publ.*, 245(1), 109–141.
- Ehlers, T. A. (2005), Crustal thermal processes and the interpretation of thermochronometer data, *Rev. Mineral. Geochem.*, 58(1), 315–350, doi:10.2138/rmg.2005.58.12.
- Ehlers, T. A., P. A. Armstrong, and D. S. Chapman (2001), Normal fault thermal regimes and the interpretation of low-temperature thermochronometers, *Phys. Earth Planet. Inter.*, 126(3), 179–194.
- Elliott, J., R. Walters, P. England, J. A. Jackson, Z. Li, and B. Parsons (2010), Extension on the Tibetan plateau: Recent normal faulting measured by InSAR and body wave seismology, *Geophys. J. Int.*, 183, 503–535, doi:10.1111/j.1365-246X.2010.04754.x.
- Ellis, S., and B. Stöckhert (2004), Elevated stresses and creep rates beneath the brittle-ductile transition caused by seismic faulting in the upper crust, *J. Geophys. Res.*, 109, B05407, doi:10.1029/2003JB002744.
- England, P., and G. Houseman (1988), The mechanics of the Tibetan Plateau, *Philos. Trans. R. Soc. London, Ser. A*, 326, 301–320.
- England, P., G. Houseman, and L. Sonder (1985), Length scales for continental deformation in convergent, divergent, and strike-slip environments: Analytical and approximate solutions for a thin viscous sheet model, *J. Geophys. Res.*, 90(B5), 3551–3557.
- Fitzgerald, P. G., E. M. Duebendorfer, J. E. Faulds, and P. O'Sullivan (2009), South Virgin–White Hills detachment fault system of SE Nevada and NW Arizona: Applying apatite fission track thermochronology to constrain the tectonic evolution of a major continental detachment fault, *Tectonics*, 28, TC2001, doi:10.1029/2007TC002194.
- Fletcher, J. M., and R. M. Spelz (2009), Patterns of Quaternary deformation and rupture propagation associated with an active low-angle normal fault, Laguna Salada, Mexico: Evidence of a rolling hinge?, *Geosphere*, 5(4), 385–407, doi:10.1130/GES00206.1.
- Förster, A., and H.-J. Förster (2000), Crustal composition and mantle heat flow: Implications from surface heat flow and radiogenic heat production in the Variscan Erzgebirge (Germany), *J. Geophys. Res.*, 105, 27,917–27,938.
- Forsyth, D. W. (1992), Finite extension and low-angle normal faulting, *Geology*, 20(1), 27–30, doi:10.1130/0091-7613(1992)020<0027.
- Francheteau, J., C. Jaupart, S. X. Jie, K. Wen-Hua, L. De-Lu, B. Jia-Chi, W. Hung-Pin, and D. Hsia-Yeu (1984), High heat flow in southern Tibet, *Nature*, 307(5), 32–36.
- Friedmann, S. J., and D. W. Burbank (1995), Rift basins and supradetachment basins: intracontinental extensional end-members, *Basin Res.*, 7(2), 109–127.
- Gan, W., P. Zhang, Z.-K. Shen, Z. Niu, M. Wang, Y. Wan, D. Zhou, and J. Cheng (2007), Present-day crustal motion within the Tibetan Plateau inferred from GPS measurements, *J. Geophys. Res.*, 112, B08416, doi:10.1029/2005JB004120.
- Garzione, C. N., P. G. DeCelles, D. G. Hodkinson, T. P. Ojha, and B. N. Upreti (2003), East-west extension and Miocene environmental change in the southern Tibetan plateau: Thakkholha graben, central Nepal, *Geol. Soc. Am. Bull.*, 115(1), 3–20.
- Hager, C., D. Stockli, T. Dewane, L. Ding, M. Taylor, and J. Lee (2006), Episodic Mio-Pliocene rifting in south-central Tibet. Thermochronometric constraints from the Xainza rift, *Eos. Trans. AGU*, 87(52), Fall Meet. Suppl., Abstract T34C-02.
- Harrison, T., P. Copeland, and W. Kidd (1995), Activation of the Nyainqntanghla shear zone: Implications for uplift of the southern Tibetan Plateau, *Tectonics*, 14(3), 658–676.
- Hedin, S. A. (1909), *Trans-Himalaya: Discoveries and Adventures in Tibet*, Macmillan, London.
- Hirm, A., M. Jiang, M. Sapin, J. Diaz, and A. Nercessian (1995), Seismic anisotropy as an indicator of mantle flow beneath the Himalayas and Tibet, *Nature*, 375, 571–574.
- Hreinsdóttir, S., and R. A. Bennett (2009), Active aseismic creep on the Alto Tiberina low-angle normal fault, Italy, *Geology*, 37(8), 683–686, doi:10.1130/G30194A.1.
- Hu, S., L. He, and J. Wang (2000), Heat flow in the continental area of China: A new data set, *Earth Planet. Sci. Lett.*, 179, 407–419.
- Jackson, S. E., N. J. Pearson, W. L. Griffin, and E. A. Belousova (2004), The application of laser ablation-inductively coupled plasma-mass spectrometry to in situ U-Pb zircon geochronology, *Chem. Geol.*, 211(1–2), 47–69, doi:10.1016/j.chemgeo.2004.06.017.
- Jaupart, C., S. Labrosse, and J.-C. Marechal (2007), Temperatures, heat and energy in the mantle of the Earth, in *Treatise on Geophysics*, vol. 7, edited by G. Schubert and D. Bercovici, pp. 254–303, Elsevier.
- Jessup, M. J., D. L. Newell, J. M. Cottle, A. L. Berger, and J. A. Spotila (2008), Orogen-parallel extension and exhumation enhanced by denudation in the trans-Himalayan Arun River gorge, Ama Drime Massif, Tibet-Nepal, *Geology*, 36(7), 587–590, doi:10.1130/G24722A.1.
- John, B. E. (1987), Geometry and evolution of a mid-crustal extensional fault system: Chemehuevi Mountains, southeastern California, in *Continental Extension Tectonics*, edited by M. P. Coward, J. F. Dewey and P. L. Hancock, *Geol. Soc. London Spec. Publ.*, 28, 313–335.
- Kapp, J., T. Harrison, P. Kapp, M. Grove, O. M. Lovera, and L. Ding (2005a), Nyainqntanghla Shan: A window into the tectonic, thermal, and geochemical evolution of the Lhasa block, southern Tibet, *J. Geophys. Res.*, 110, B08413, doi:10.1029/2004JB003330.
- Kapp, P., A. Yin, T. M. Harrison, and L. Ding (2005b), Cretaceous-Tertiary shortening, basin development, and volcanism in central Tibet, *Geol. Soc. Am. Bull.*, 117(7/8), 865–878, doi:10.1130/B25595.1.
- Kapp, P., P. DeCelles, G. Gehrels, M. Heizler, and L. Ding (2007), Geological records of the Lhasa-Qiangtang and Indo-Asian collisions in the Nima area of central Tibet, *Geol. Soc. Am. Bull.*, 119(7–8), 917–932, doi:10.1130/B26033.1.
- Kapp, P. A., M. H. Taylor, and D. F. Stockli (2008), Development of active low-angle normal fault systems during orogenic collapse: Insight from Tibet, *Geology*, 36(1), 7–10, doi:10.1130/G24054A.1.
- Ketcham, R. A. (1996), Thermal models of core-complex evolution in Arizona and New Guinea: Implications for ancient cooling paths and present-day heat flow, *Tectonics*, 15(5), 933–951.
- Ketcham, R. A. (2005), Forward and inverse modeling of low-temperature thermochronometry data, *Rev. Mineral.*, 58, 275–314, doi:10.2138/rmg.2005.58.11.
- Klootwijk, C., P. Conaghan, and C. M. A. Powell (1985), The Himalayan Arc: Large-scale continental subduction, oroclininal bending and back-arc spreading, *Earth Planet. Sci. Lett.*, 75(2–3), 167–183.
- Kogan, L., S. Fisseha, R. Bendick, R. E. Reilinger, S. McClusky, B. King, and T. Solomon (2012), Lithospheric strength and strain localization in continental extension from observations of the East African Rift, *J. Geophys. Res.*, 117, B03402, doi:10.1029/2011JB008516.
- Kong, X., and P. Bird (1996), Neotectonics of Asia: Thin-shell finite-element models with faults, in: *The Tectonic Evolution of Asia*, edited by A. Yin and T. M. Harrison, pp. 18–34, Cambridge Univ. Press, Cambridge, UK.
- Lacassin, R., et al. (2004), Large-scale geometry, offset and kinematic evolution of the Karakorum fault, Tibet, *Earth Planet. Sci. Lett.*, 219(3–4), 255–269, doi:10.1016/S0012-821X(04)00006-8.
- Langille, J. M., M. J. Jessup, J. M. Cottle, D. Newell, and G. Seward (2010), Kinematic evolution of the Ama Drime detachment: insights into orogen-parallel extension and exhumation of the Ama Drime Massif, Tibet-Nepal, *J. Struct. Geol.*, 32(7), 900–919, doi:10.1016/j.jsg.2010.04.005.
- Lease, R. O., D. W. Burbank, M. K. Clark, K. A. Farley, D. Zheng, and H. Zhang (2011), Middle Miocene reorganization of deformation along the northeastern Tibetan Plateau, *Geology*, 39(4), 359–362, doi:10.1130/G31356.1.
- Lee, J., and G. S. Lister (1992), Late Miocene ductile extension and detachment faulting, Mykonos, Greece, *Geology*, 20(2), 121–124.
- Lee, J., E. L. Miller, and J. F. Sutter (1987), Ductile strain and metamorphism in an extensional tectonic setting: A case study from the northern Snake Range, Nevada, USA, in *Continental Extensional Tectonics*, edited by M. P. Coward, J. F. Dewey, and P. L. Hancock, pp. 267–298, Geological Society of London Special Publications, 28.
- Lee, J., C. Hager, S. R. Wallis, D. F. Stockli, M. J. Whitehouse, M. Aoya, and Y. Wang (2011), Middle to late Miocene extremely rapid exhumation and thermal reequilibration in the Kung Co rift, southern Tibet, *Tectonics*, 30, TC2007, doi:10.1029/2010TC002745.
- Lister, G. S., and G. A. Davis (1989), The origin of metamorphic core complexes and detachment faults formed during Tertiary continental extension in the northern Colorado River region, USA, *J. Struct. Geol.*, 11(1–2), 65–94.
- Liu, C.-Z., F.-Y. Wu, S.-L. Chung, and Z.-D. Zhao (2011), Fragments of hot and metasomatized mantle lithosphere in Middle Miocene

- ultrapotassic lavas, southern Tibet, *Geology*, 39(10), 923–926, doi:10.1130/G32172.1.
- Leloup, P. H., G. Mahéo, N. Arnaud, E. Kali, E. Boutonnet, D. Liu, X. Liu, and H. Li (2010), The South Tibet detachment shear zone in the Dinggye area: Time constraints on extrusion models of the Himalayas, *Earth Planet. Sci. Lett.*, 292(1), 1–16.
- Loveless, J. P., and B. J. Meade (2011), Partitioning of localized and diffuse deformation in the Tibetan Plateau from joint inversions of geologic and geodetic observations TS AT, *Earth Planet. Sci. Lett.*, 303(1–2), 11–24, doi:10.1016/j.epsl.2010.12.014.
- Mahéo, G., P. H. Leloup, F. Valli, R. Lacassin, N. Arnaud, and J. Paquette (2007), Post 4 Ma initiation of normal faulting in southern Tibet: Constraints from the Kung Co half graben, *Earth Planet. Sci. Lett.*, 256, 233–243, doi:10.1016/j.epsl.2007.01.029.
- Masek, J. G., B. L. Isacks, E. J. Fielding, and J. Browaeys (1994), Rift flank uplift in Tibet: Evidence for a viscous lower crust, *Tectonics*, 13(3), 659–667.
- McNulty, B., and D. Farber (2002), Active detachment faulting above the Peruvian flat slab, *Geology*, 30(6), 567–570.
- Meade, B. J. (2007), Present-day kinematics at the India-Asia collision zone, *Geology*, 35, 81–84.
- Mechie, J., S. V. Sobolev, L. Ratschbacher, A. Y. Babeyko, G. Bock, A. G. Jones, K. D. Nelson, K. D. Solon, L. D. Brown, and W. Zhao (2004), Precise temperature estimation in the Tibetan crust from seismic detection of the  $\alpha$ - $\beta$  quartz transition, *Geology*, 32(7), 601–604, doi:10.1130/G20367.1.
- Meigs, A. J., D. W. Burbank, and R. A. Beck (1995), Middle-late Miocene (>10 Ma) formation of the Main Boundary thrust in the western Himalaya, *Geology*, 23(5), 423–426, doi:10.1130/0091-7613(1995)023<0423.
- Molnar, P., and W.-P. Chen (1983), Focal depths and fault plane solutions of earthquakes under the Tibetan plateau, *J. Geophys. Res.*, 88(B2), 1180–1196.
- Molnar, P., and H. Lyon-Caen (1989), Fault plane solutions of earthquakes and active tectonics of the Tibetan Plateau and its margins, *Geophys. J. Int.*, 99, 123–153.
- Molnar, P., and J. M. Stock (2009), Slowing of India's convergence with Eurasia since 20 Ma and its implications for Tibetan mantle dynamics, *Tectonics*, 28, TC3001, doi:10.1029/2008TC002271.
- Molnar, P., and P. Tapponnier (1975), Cenozoic tectonics of Asia: effects of a continental collision, *Science*, 189(4201), 419–426.
- Molnar, P., P. England, and J. Martinod (1993), Mantle dynamics, uplift of the Tibetan Plateau, and the Indian monsoon, *Rev. Geophys.*, 31(4), 357–396.
- Morley, C. K. (1999), Marked along-strike variations in dip of normal faults—the Lokichar fault, N. Kenya rift: a possible cause for metamorphic core complexes, *J. Struct. Geol.*, 21, 479–492.
- Morley, C. K. (2009), Geometry and evolution of low-angle normal faults (LANF) within a Cenozoic high-angle rift system, Thailand: Implications for sedimentology and the mechanisms of LANF development, *Tectonics*, 28, TC5001, doi:10.1029/2007TC002202.
- Murphy, M. (2007), Isotopic characteristics of the Gurla Mandhata metamorphic core complex: Implications for the architecture of the Himalayan orogen, *Geology*, 35(11), 983–986, doi:10.1130/G23774A.1.
- Murphy, M., A. Yin, T. Harrison, S. Dürr, Z. Chen, F. J. Ryerson, W. S. F. Kidd, X. Wang, and X. Zhou (1997), Did the Indo-Asian collision alone create the Tibetan plateau?, *Geology*, 25(8), 719–722.
- Murphy, M. A., A. Yin, P. Kapp, T. M. Harrison, C. E. Manning, F. J. Ryerson, D. Lin, and G. Jinghui (2002), Structural evolution of the Gurla Mandhata detachment system, southwest Tibet: Implications for the eastward extent of the Karakoram fault system, *Geol. Soc. Am. Bull.*, 114(4), 428–447.
- Murphy, M., V. Sanchez, and M. Taylor (2010), Syncollisional extension along the India-Asia suture zone, south-central Tibet: Implications for crustal deformation of Tibet, *Earth Planet. Sci. Lett.*, 290(3–4), 233–243, doi:10.1016/j.epsl.2009.11.046.
- Nábelek, J., G. Hetényi, J. Vergne, S. Sapkota, B. Kafle, M. Jiang, H. Su, J. Chen, and B.-S. Huang (2009), Underplating in the Himalaya-Tibet collision zone revealed by the Hi-CLIMB experiment, *Science*, 325(5946), 1371–1374, doi:10.1126/science.1167719.
- Nelson, K. D., et al. (1996), Partially molten middle crust beneath southern Tibet: Synthesis of project INDEPTH results, *Science*, 274(5293), 1684–1688.
- Niemi, N. A., B. P. Wernicke, A. M. Friedrich, M. Simons, R. A. Bennett, and J. L. Davis (2004), BARGEN continuous GPS data across the eastern Basin and Range province, and implications for fault system dynamics, *Geophys. J. Int.*, 159(3), 842–862, doi:10.1111/j.1365-246X.2004.02454.x.
- Owens, T. J., and G. Zandt (1997), Implications of crustal property variations for models of Tibetan plateau evolution, *Nature*, 387(6628), 37–43.
- Pan, Y., and W. Kidd (1992), Nyainqntanglha shear zone: A late Miocene extensional detachment in the southern Tibetan Plateau, *Geology*, 20(9), 775–778, doi:10.1130/0091-7613(1992)020<0775.
- Parsons, T., and G. A. Thompson (1993), Does magmatism influence low-angle normal faulting?, *Geology*, 21(3), 247–250.
- Paton, C., J. Hellstrom, B. Paul, J. Woodhead, and J. Herjt (2011), Iolite: Freeware for the visualisation and processing of mass spectrometric data, *J. Anal. At. Spectrom.*, 26, 2508–2518, doi:10.1039/c1ja0172b.
- Petrus, J. A., and Kamber, B. S. (2012), VizualAge: A novel approach to laser ablation ICP-MS U-Pb geochronology data reduction, *Geostand. Geoanal. Res.*, 36(3), 247–270, doi: 10.1111/j.1751-908X.2012.00158.x.
- Priestley, K., J. Jackson, and D. McKenzie (2008), Lithospheric structure and deep earthquakes beneath India, the Himalaya and southern Tibet, *Geophys. J. Int.*, 172, 345–362, doi:10.1111/j.1365-246X.2007.03636.x.
- Ratschbacher, L., I. Krumrei, M. Blumenwitz, M. Staiger, R. Gloaguen, B. V. Miller, S. D. Samson, M. A. Edwards, and E. Appel (2011), Rifting and strike-slip shear in central Tibet and the geometry, age and kinematics of upper crustal extension in Tibet, *Geol. Soc. Spec. Publ.*, 353(1), 127–163, doi:10.1144/SP353.8.
- Reiners, P. (2005), Zircon (U-Th)/He thermochronometry, *Rev. Mineral. Geochem.*, 58(1936), 151–179, doi:10.2138/rmg.2005.58.6.
- Rey, P., C. Teyssier, and D. Whitney (2009), The role of partial melting and extensional strain rates in the development of metamorphic core complexes, *Tectonophysics*, 477(3–4), 135–144, doi:10.1016/j.tecto.2009.03.010.
- Robinson, A. C., A. Yin, C. E. Manning, T. M. Harrison, S.-H. Zhang, and X. F. Wang (2004), Tectonic evolution of the northeastern Pamir: Constraints from the northern portion of the Cenozoic Kongur Shan extensional system, western China, *Geol. Soc. Am. Bull.*, 116(7–8), 953–973, doi:10.1130/B25375.1.
- Robinson, D. M., P. G. DeCelles, and P. Copeland (2006), Tectonic evolution of the Himalayan thrust belt in western Nepal: Implications for channel flow models, *Geol. Soc. Am. Bull.*, 118(7/8), 865–885.
- Robinson, A. C., A. Yin, and O. M. Lovera (2010), The role of footwall deformation and denudation in controlling cooling age patterns of detachment systems: An application to the Kongur Shan extensional system in the Eastern Pamir, China, *Tectonophysics*, 496(1–4), 28–43, doi:10.1016/j.tecto.2010.10.003.
- Ross, S. M., (2003), Peirce's criterion for the elimination of suspect experimental data, *J. Eng. Technol.*, 20(2), 38–41.
- Ryder, I., R. Bürgmann, and E. J. Fielding (2012), Static stress interactions in extensional earthquake sequences: an example from the South Lunggar Rift, Tibet, *J. Geophys. Res.*, 117, B09405, doi:10.1029/2012JB009365.
- Sanchez, V. I., M. A. Murphy, A. A. C. Robinson, T. J. Lapen, and M. T. Heizler (2013), Tectonic evolution of the India-Asia suture zone since Middle Eocene time, Lopukangri area, south-central Tibet. *J. Asian Earth Sci.*, 62, 205–220, doi:10.1016/j.jseas.2012.09.004.
- Saylor, J., P. DeCelles, G. Gehrels, M. Murphy, R. Zhang, and P. Kapp (2010), Basin formation in the High Himalaya by arc-parallel extension and tectonic damming: Zhada basin, southwestern Tibet, *Tectonics*, 29, TC1004, doi:10.1029/2008TC002390.
- Searle, M. P., J. R. Elliott, and R. J. Phillips (2011), Lithospheric structure and continental extrusion of Tibet, *J. Geol. Soc. London*, 168, 633–672, doi:10.1144/0016-76492010-139.
- Sibson, R. H. (1983), Continental fault structure and the shallow earthquake source, *J. Geol. Soc.*, 140(5), 741–767.
- Spencer, J. E. (1984), Role of tectonic denudation in warping and uplift of low-angle normal faults, *Geology*, 12(2), 95–98.
- Spencer, J. (2010), Structural analysis of three extensional detachment faults with data from the 2000 Space-Shuttle Radar Topography Mission, *GSA Today*, 8, 4–10, doi:10.1130/GSATG59A.1.
- Stockli, D. F. (2005), Application of low-temperature thermochronometry to extensional tectonic settings, *Rev. Mineral. Geochem.*, 58, 411–448, doi:10.2138/rmg.2005.58.16.
- Stockli, D. F., B. E. Surpless, T. A. Dumitru, and K. A. Farley (2002), Thermochronological constraints on the timing and magnitude of Miocene and Pliocene extension in the central Wassuk Range, western Nevada, *Tectonics*, 21(4), 1028–1038.
- Styron, R., M. Taylor, and K. Okoronkwo (2010), Database of active structures from the Indo-Asian Collision, *Eos. Trans. AGU*, 91(20), 181–182, doi:10.1130/GES00217.1.
- Styron, R. H., M. H. Taylor, and M. A. Murphy (2011a), Oblique convergence, arc-parallel extension, and the role of strike-slip faulting in the High Himalaya, *Geosphere*, 7(2), 582–596, doi:10.1130/GES00606.1.
- Styron, R., M. Taylor, K. Sundell, D. Stockli, A. McCallister, D. Liu, and L. Ding (2011b), Variations in extensional style in the Lunggar Rift, Southern Tibet, through a change in extensional driving forces, *Eos. Trans. AGU*, 92(52), Fall Meet. Suppl., T43F-2457.
- Taylor, M., A. Yin, F. J. Ryerson, P. Kapp, and L. Ding (2003), Conjugate strike-slip faulting along the Bangong-Nujiang suture zone accommodates coeval east-west extension and north-south shortening in the interior of the Tibetan Plateau, *Tectonics*, 22(4), 1044, doi:10.1029/2002TC001361.
- Thatcher, W. (2007), Microplate model for the present-day deformation of Tibet, *J. Geophys. Res.*, 112, B01401, doi:10.1029/2005JB004244.

- Thiede, R. C., J. R. Arrowsmith, B. Bookhagen, M. McWilliams, E. R. Sobel, and M. R. Strecker (2006), Dome formation and extension in the Tethyan Himalaya, Leo Pargil, northwest India, *Bull. Geol. Soc. Am.*, 118(5–6), 635–650, doi:10.1130/B25872.1.
- Tirel, C., J.-P. Brun, and E. Burov (2008), Dynamics and structural development of metamorphic core complexes, *J. Geophys. Res.*, 113, B04403, doi:10.1029/2005JB003694.
- Volkmer, J. E., P. Kapp, J. H. Guynn, and Q. Lai (2007), Cretaceous-Tertiary structural evolution of the north central Lhasa terrane, Tibet, *Tectonics*, 26, TC6007, doi:10.1029/2005TC001832.
- Wang, Y. (2001), Heat flow pattern and lateral variations of lithosphere strength in China mainland: Constraints on active deformation, *Phys. Earth Planet. Inter.*, 126(3–4), 121–146, doi:10.1016/S0031-9201(01)00251-5.
- Wdowinski, S., and G. J. Axen (1992), Isostatic rebound due to tectonic denudation: A viscous flow model of a layered lithosphere, *Tectonics*, 11(2), 303–315.
- Wei, S., et al. (2010), Regional earthquakes in northern Tibetan Plateau: Implications for lithospheric strength in Tibet, *Geophys. Res. Lett.*, 37, L19307, doi:10.1029/2010GL044800.
- Wernicke, B. (1981), Low-angle normal faults in the Basin and Range Province: Nappe tectonics in an extending orogen, *Nature*, 291, 645–648.
- Wernicke, B. (1995), Low-angle normal faults and seismicity: A review, *J. Geophys. Res.*, 100(B10), 20,159–20,174.
- Wernicke, B., and G. J. Axen (1988), On the role of isostasy in the evolution of normal fault systems, *Geology*, 16, 848–851.
- Wessel, P., and W. H. Smith (1996), A global, self-consistent, hierarchical, high-resolution shoreline database, *J. Geophys. Res.*, 101(B4), 8741–8743.
- Whittington, A. G., A. M. Hofmeister, and P. I. Nábělek (2009), Temperature-dependent thermal diffusivity of the Earth's crust and implications for magmatism, *Nature*, 458(7236), 319–21, doi:10.1038/nature07818.
- Wolfe, M. R., and D. F. Stockli (2010), Zircon (U-Th)/He thermochronometry in the KTB drill hole, Germany, and its implications for bulk He diffusion kinetics in zircon, *Earth Planet. Sci. Lett.*, 295(1–2), 69–82, doi:10.1016/j.epsl.2010.03.025.
- Woodruff, W., B. K. Horton, P. Kapp, and D. F. Stockli (2013), Late Cenozoic evolution of the Lunggar extensional basin, Tibet: Implications for basin growth and exhumation in hinterland plateaus, *Geol. Soc. Am. Bull.*, 125(3–4), 343–358, doi:10.1130/B30664.1.
- Yin, A. (2000), Mode of Cenozoic east-west extension in Tibet suggesting a common origin of rifts in Asia during the Indo-Asian collision, *J. Geophys. Res.*, 105(B9), 21,745–21,759, doi:10.1029/2000JB900168.
- Yin, A. (2010), Cenozoic tectonic evolution of Asia: A preliminary synthesis, *Tectonophysics*, 488(1–4), 293–325, doi:10.1016/j.tecto.2009.06.002.
- Yin, A., and J. F. Dunn (1992), Structural and stratigraphic development of the Whipple-Chemehuevi detachment fault system, southeastern California: Implications for the geometrical evolution of domal and basinal low-angle normal faults, *Geol. Soc. Am. Bull.*, 104(6), 659–674, doi:10.1130/0016-7606(1992)104<0659.
- Yin, A., and T. M. Harrison (2000), Geologic evolution of the Himalayan-Tibetan Orogen, *Annu. Rev. Earth Planet. Sci.*, 28(1), 211–280, doi:10.1146/annurev.earth.28.1.211.
- Yin, A., and M. H. Taylor (2011), Mechanics of V-shaped conjugate strike-slip faults and the corresponding continuum mode of continental deformation, *Geol. Soc. Am. Bull.*, 123(9–10), 1798–1821, doi:10.1130/B30159.1.
- Yin, A., T. Harrison, and F. Ryerson (1994), Tertiary structural evolution of the Gangdese thrust system, southeastern Tibet, *J. Geophys. Res.*, 99(B9), 18,175–18,190.
- Zhang, P. Z., Z. Shen, M. Wang, W. Gan, R. Bürgmann, P. Molnar, Q. Wang, Z. Niu, J. Sun, and J. Wu (2004), Continuous deformation of the Tibetan Plateau from global positioning system data, *Geology*, 32(9), 809–812.
- Zhang, R., M. A. Murphy, T. J. Lapen, V. Sanchez, and M. Heizler (2011), Late Eocene crustal thickening followed by Early-Late Oligocene extension along the India-Asia suture zone: Evidence for cyclicity in the Himalayan orogen, *Geosphere*, 7(5), 1249–1268, doi:10.1130/GES00643.1.